

Photophysicochemical Processes in Host-Guest Systems and Their Applications in Energy Conversion and Synthesis

Lead Guest Editor: Elamparuthi Ramasamy

Guest Editors: Takuya Fujimura and Mahesh Pattabiraman





**Photophysicochemical Processes in Host-Guest
Systems and Their Applications in Energy
Conversion and Synthesis**

International Journal of Photoenergy

**Photophysicochemical Processes
in Host-Guest Systems and Their
Applications in Energy Conversion and
Synthesis**

Lead Guest Editor: Elamparuthi Ramasamy

Guest Editors: Takuya Fujimura and Mahesh
Pattabiraman



Copyright © 2021 Hindawi Limited. All rights reserved.

This is a special issue published in "International Journal of Photoenergy." All articles are open access articles distributed under the Creative Commons Attribution License, which permits unrestricted use, distribution, and reproduction in any medium, provided the original work is properly cited.

Chief Editor

Giulia Grancini , Italy

Academic Editors

Mohamed S.A. Abdel-Mottaleb , Egypt
Angelo Albini, Italy
Mohammad Alghoul , Malaysia
Alberto Álvarez-Gallegos , Mexico
Vincenzo Augugliaro , Italy
Detlef W. Bahnemann, Germany
Simona Binetti, Italy
Fabio Bisegna , Italy
Thomas M. Brown , Italy
Joaquim Carneiro , Portugal
Yatendra S. Chaudhary , India
Kok-Keong Chong , Malaysia
Věra Cimrová , Czech Republic
Laura Clarizia , Italy
Gianluca Coccia , Italy
Daniel Tudor Cotfas , Romania
P. Davide Cozzoli , Italy
Dionysios D. Dionysiou , USA
Elisa Isabel Garcia-Lopez , Italy
Wing-Kei Ho , Hong Kong
Siamak Hoseinzadeh, Italy
Jürgen Hüpkes , Germany
Fayaz Hussain , Brunei Darussalam
Mohamed Gamal Hussien , Egypt
Adel A. Ismail, Kuwait
Chun-Sheng Jiang, USA
Zaiyong Jiang, China
Yuanzuo Li , China
Manuel Ignacio Maldonado, Spain
Santolo Meo , Italy
Claudio Minero, Italy
Regina De Fátima Peralta Muniz Moreira ,
Brazil
Maria da Graça P. Neves , Portugal
Tsuyoshi Ochiai , Japan
Kei Ohkubo , Japan
Umapada Pal, Mexico
Dillip K. Panda, USA
Carlo Renno , Italy
Francesco Riganti-Fulginei , Italy
Leonardo Sandrolini , Italy
Jinn Kong Sheu , Taiwan
Kishore Sridharan , India

Elias Stathatos , Greece
Jegadesan Subbiah , Australia
Chaofan Sun , China
K. R. Justin Thomas , India
Koray Ulgen , Turkey
Ahmad Umar, Saudi Arabia
Qiliang Wang , China
Xuxu Wang, China
Huiqing Wen , China
Wei jie Yang , China
Jiangbo Yu , USA

Contents

Ni-Doped Protonated Layered Titanate/TiO₂ Composite with Efficient Photocatalytic Activity for NO_x Decomposition Reactions

Kanji Saito , Shota Oriksa, Yusuke Asakura , Yusuke Ide , Yoshiyuki Sugahara , Masataka Ogasawara , Shu Yin , and Sumio Kato 

Research Article (9 pages), Article ID 8847956, Volume 2021 (2021)

Guest-Host Interactions in Symmetrical Carboxy Heptamethine Cyanine Dyes-Titanium Dioxide Systems: Synthesis, Theoretical Calculations, Aggregation Properties, and Application in Dye-Sensitized Solar Cells

Rodrigo da Costa Duarte , Matheus Costa de Oliveira, Josene Maria Toldo , Paulo Fernando Bruno Gonçalves , Marcos José Leite Santos , and Fabiano Severo Rodembusch 

Research Article (17 pages), Article ID 8852979, Volume 2021 (2021)

Preparation of Transparent Film of Layered Double Hydroxide with Anionic Pyrene Derivatives and Its Luminous Toluene Detection Ability

Takuya Fujimura , Yoshiya Akagashi, Yu-hei Aoyama, and Ryo Sasai 

Research Article (7 pages), Article ID 8870930, Volume 2020 (2020)

Research Article

Ni-Doped Protonated Layered Titanate/TiO₂ Composite with Efficient Photocatalytic Activity for NO_x Decomposition Reactions

Kanji Saito ^{1,2}, Shota Orikasa,³ Yusuke Asakura ⁴, Yusuke Ide ⁵,
Yoshiyuki Sugahara ^{2,6}, Masataka Ogasawara ¹, Shu Yin ⁴ and Sumio Kato ¹

¹Department of Materials Science, Graduate School of Engineering Science, Akita University, 1-1 Tegatagakuen-machi, Akita-shi, Akita 010-8502, Japan

²Kagami Memorial Research Institute for Materials Science and Technology, Waseda University, 2-8-26 Nishiwaseda, Shinjuku-ku, Tokyo 169-0054, Japan

³Faculty of Engineering Science, Akita University, 1-1 Tegatagakuen-machi, Akita-shi, Akita 010-8502, Japan

⁴Institute of Multidisciplinary Research for Advanced Materials (IMRAM), Tohoku University, 2-1-1 Katahira, Aoba-ku, Sendai 980-8577, Japan

⁵International Center for Materials Nanoarchitectonics (WPI-MANA), National Institute for Materials Science (NIMS), 1-1 Namiki, Tsukuba, Ibaraki 305-0044, Japan

⁶Department of Applied Chemistry, School of Advanced Science and Engineering, Waseda University, 3-4-1 Okubo, Shinjuku-ku, Tokyo 169-8555, Japan

Correspondence should be addressed to Kanji Saito; saitok@gipc.akita-u.ac.jp

Received 11 September 2020; Accepted 7 January 2021; Published 28 January 2021

Academic Editor: Elamparuthi Ramasamy

Copyright © 2021 Kanji Saito et al. This is an open access article distributed under the Creative Commons Attribution License, which permits unrestricted use, distribution, and reproduction in any medium, provided the original work is properly cited.

A unique structural transformation of a lepidocrocite-type layered titanate, K_{0.8}Ti_{1.73}Li_{0.27}O₄, into a rutile-type TiO₂ has recently been realized *via* dilute HCl treatment and subsequent drying at room temperature for producing rutile-nanoparticle-decorated protonated layered titanate exhibiting highly efficient photocatalytic activity. Herein, the authors report synthesis of a lepidocrocite-type layered cesium titanate with nominal compositions of Cs_{0.7}Ti_{1.825-x/2}Ni_x□_{0.175-x/2}O₄ ($x = 0, 0.05, 0.1,$ and 0.35) through solid-state reactions of Cs₂CO₃, TiO₂, and Ni(CH₃COO)₂·4H₂O at different temperatures (600 or 800°C), followed by treatment with dilute HCl and subsequent drying to produce a Ni-doped protonated layered titanate/TiO₂ composite. Cs_{0.7}Ti_{1.825-x/2}Ni_x□_{0.175-x/2}O₄ with an optimized Ni content obtained at a lower temperature was converted into a Ni-doped protonated layered titanate/TiO₂ composite to exhibit high photocatalytic activity for NO_x decomposition reactions.

1. Introduction

Fuel production, environmental purification, and fine chemical synthesis using a semiconductor photocatalyst with solar light have attracted tremendous attention for developing sustainable photoenergy conversion processes [1–5]. Efforts have thus been made to modify conventional semiconductor photocatalysts as well as to synthesize new state-of-the-art versions, in terms of improved charge-separation efficiency, photoabsorption properties, and specific surface area. Layered transition metal oxides have been used to design highly efficient photocatalysts, due to their ability to provide

expandable 2D nanospaces to accommodate reactants and such functional species as cocatalysts and sensitizers [6–8]. The interlayer structures have been controlled to induce unique photocatalytic reactions, moreover, such as substrates or product-selective reactions [9, 10].

Among layered transition metal oxides, lepidocrocite-type layered titanates are characterized by swelling properties as well as compositional versatility [11]. These make them extremely promising candidates for designing highly efficient functional hybrid photocatalysts. The general formula for lepidocrocite-type layered titanate is A_xTi_{2-y}M_yO₄ (A: interlayer alkali metal ion; M: metal ion or vacancy). Alkali metal

ions are located in the interlayer spaces between titanate sheets to compensate for the negative charge of the layers, which arises from isomorphous substitution of Ti with low-valent metal species or vacancies. We recently reported that a lepidocrocite-type layered titanate with a composition of $K_{0.8}Ti_{1.73}Li_{0.27}O_4$ (referred to as "KTLO") exhibited a unique transformation into rutile with dilute HCl treatment and subsequent drying at room temperature (even at 60°C to accelerate the transformation) [12, 13]. Rutile nanoparticles were formed on the outer surface (not in the interlayer space) of protonated layered titanate particles ($H_{1.07}Ti_{1.73}\square_{0.27}O_4$; \square denotes a vacancy) during the drying process. After Pt loading, the protonated layered titanate/rutile composite showed higher photocatalytic H_2 evolution activity from water when compared with Pt-loaded P25 (a benchmark photocatalyst for the reaction). The high photocatalytic activity was explained by a transfer of photoexcited electrons from the protonated layered titanate phase to rutile for enhancing charge separation efficiency. It should be noted that photocatalytic activity of the protonated layered titanate was remarkably enhanced without any interlayer modification, which often requires multiple complicated steps.

Doping of transition metal ions into a TiO_2 framework often results in improved photocatalytic activity due to enhanced-charge separation efficiency and/or development of visible-light responsivity [14–19]. In the case of acid treatment of KTLO, the Li^+ ions in the layers were completely extracted to leave defects in the titanate sheet [12], while the negative charge was likely to be balanced by accommodating H^+ (or in the form of H_3O^+). On the other hand, negligible extraction of Ni^{2+} was observed for $Cs_{0.7}Ti_{1.65}Ni_{0.35}O_4$ under the same experimental conditions as those for KTLO, possibly due to a stronger electrostatic interaction between metal ions with higher valences and oxide anions [20]. In the present study, we selected Ni-doped lepidocrocite-type layered cesium titanates with different Ni contents as starting materials, and the effects of the Ni-doping on the photocatalytic activity of the layered cesium titanate after dilute HCl treatment and subsequent drying for NO_x decomposition reactions was investigated.

2. Experimental

2.1. Materials. Potassium carbonate (K_2CO_3 , 99.95%) was purchased from Kanto Chemical Co., Ltd. Cesium carbonate (Cs_2CO_3 , 95.0–102%) and nickel acetate tetrahydrate ($Ni(CH_3COO)_2 \cdot 4H_2O$, 98.0%) were obtained from FUJIFILM Wako Pure Chemical Corporation. Titanium dioxide (P25 TiO_2 , $\geq 99.5\%$) was kindly donated by Nippon Aerosil Co., Ltd. Anatase-type TiO_2 (JRC-TIO-1) and rutile-type TiO_2 (JRC-TIO-16) were supplied by the Catalysis Society of Japan. Hydrochloric acid (HCl, 35.0–37.0%) was purchased from Nacalai Tesque, Inc.

2.2. Sample Preparation. A layered cesium titanate with nominal compositions of $Cs_{0.7}Ti_{1.825-x/2}Ni_x\square_{0.175-x/2}O_4$ ($x = 0, 0.05, 0.1, \text{ and } 0.35$) was synthesized by solid-state reactions with stoichiometric ratios of Cs_2CO_3 , TiO_2 , and $Ni(CH_3COO)_2 \cdot 4H_2O$. TiO_2 was suspended in an aqueous solution of Cs_2CO_3 with/without $Ni(CH_3COO)_2 \cdot 4H_2O$ by ultrasoni-

cation for 5 min, and the suspension was stirred at 100°C to evaporate the water. The powder mixture was collected and then calcined at 600°C for 30 min in air. After cooling to room temperature, the sample was mixed again with acetone using a planetary ball mill (Planet M2-3, Gokin Planetaring Inc.). After evaporation of the acetone at room temperature, the samples were calcined at 600°C or 800°C for 20 h in air. The samples obtained by the solid-state reactions were referred to as CTNO (x) $_T$, where T represents the calcination temperature. CTNO (x) $_T$ was suspended in dilute HCl (0.5 M), and the suspension was stirred at room temperature for 3 days. After centrifugation, the solid phase was collected and dried at 60°C overnight without washing with water, resulting in retention of HCl on the outer particle surface. The samples prepared by dilute HCl treatment and subsequent drying of CTNO (x) $_T$ were referred to as HTNO (x) $_T$.

2.3. Characterization. X-ray powder diffraction (XRD) patterns of the samples were recorded with a Rigaku Ultima IV diffractometer operated at 40 mA and 40 kV with monochromatic $CuK\alpha$ radiation. UV-vis diffuse reflectance (UV-vis DR) spectra of the samples were obtained with a JASCO V-750 spectrophotometer equipped with an integrating sphere (ISV-722 attachment). X-ray photoelectron spectroscopy (XPS) analyses were performed with an ULVAC-PHI PHI5600. Raman spectra were recorded with a Renishaw in Via reflex spectrometer using a 532 nm laser. Inductively coupled plasma atomic emission spectroscopy (ICP-AES) measurement was performed with an SPS 5510 (SII Nano-Technology, Inc.). The extraction rate (%) of Ti and Ni from the samples during the dilute HCl treatment was determined by the following equation:

$$\text{Extraction rate (\%)} = \frac{\text{Amount of element extracted}}{\text{Amount of element in the sample}} \times 100 \quad (1)$$

2.4. Photocatalytic Reaction. The photocatalytic activity of the samples was evaluated by a NO_x decomposition reaction in the gas phase under light irradiation ($\lambda > 290$ nm) at room temperature using a continuous flow-type reactor. A high-pressure mercury lamp (Ushio 450 W) was used as a light source. The initial concentration of NO was set to 1 ppm with compressed air, and the NO_x concentration after photocatalytic decomposition was estimated using an NO_x analyzer (Yanaco, ECL-88A). Note that NO_2 formed by photocatalytic oxidation of NO is also counted as an NO_x species. The NO conversion ratio was calculated using the measured NO_x concentration.

3. Results and Discussions

Figure 1 shows XRD patterns of CTNO (0) $_800$, CTNO (0.05) $_800$, HTNO (0) $_800$, and HTNO (0.05) $_800$. Note that the layered cesium titanate with a composition of $Cs_{0.7}Ti_{1.825}\square_{0.175}O_4$, which is equivalent to the nominal composition of CTNO (0) $_800$, has previously been prepared by a solid-state reaction of Cs_2CO_3 and TiO_2 at above 700°C.

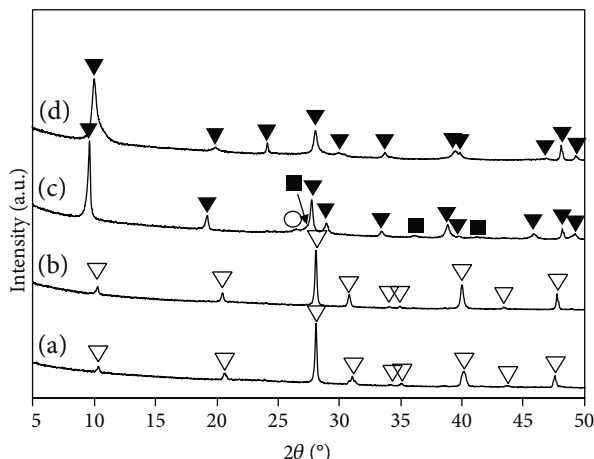


FIGURE 1: XRD patterns of (a) CTNO (0)_800, (b) CTNO (0.05)_800, (c) HTNO (0)_800, and (d) HTNO (0.05)_800: ▽: $\text{Cs}_{0.7}\text{Ti}_{1.825}\square_{0.175}\text{O}_4$, ▼: $\text{H}_{0.7}\text{Ti}_{1.825}\square_{0.175}\text{O}_4$, ■: TiO_2 (rutile), and ○: unknown.

Both the XRD patterns of CTNO (0)_800 and CTNO (0.05)_800 (Figures 1(a) and 1(b)) were assignable to that of $\text{Cs}_{0.7}\text{Ti}_{1.825}\square_{0.175}\text{O}_4$ [21], indicating that layered cesium titanate with/without Ni was successfully obtained. The visible-light absorption at a wavelength shorter than 500 nm by Ni addition (Figure 2) supports successful Ni-doping into the titanate sheet framework, since transition metals including Ni can develop visible-light absorption by formation of localized energy states in the band gap of TiO_2 [14] and since the local structure of lepidocrocite-type layered titanates is similar to that of TiO_2 [22]. The tail of the visible-light absorption was located at a position closely similar to that observed for Ni-doped TiO_2 in previous reports [23, 24]. In the XRD pattern of HTNO (0)_800 (Figure 1(c)), peaks attributable to rutile were observed at $2\theta = 27.4, 36.1,$ and 41.2° , while peaks in other positions were assignable to $\text{H}_{0.7}\text{Ti}_{1.825}\square_{0.175}\text{O}_4$ [21], the protonated form of $\text{Cs}_{0.7}\text{Ti}_{1.825}\square_{0.175}\text{O}_4$, revealing that the partial transformation of titanate sheets to rutile observed for KTLO in the previous report also occurred in CTNO (0)_800. On the other hand, no rutile formation was observed in HTNO (0.05)_800 (Figure 1(d)), indicating that doping with a small Ni content suppressed the transformation of the titanate sheets into rutile.

Figure 3(a) shows XRD patterns of CTNO (x)_600. Although a very weak XRD peak ascribable to anatase was observed at $2\theta = 25.4^\circ$, the XRD pattern of CTNO (0)_600 was almost identical to that of $\text{Cs}_{0.7}\text{Ti}_{1.825}\square_{0.175}\text{O}_4$ [21]. This indicates that $\text{Cs}_{0.7}\text{Ti}_{1.825}\square_{0.175}\text{O}_4$ was obtained even at 600°C , while it has been prepared by solid-state reactions only at above 700°C [21, 25–28]. Weak peaks at $2\theta = 25.4^\circ$ ascribable to anatase were observed in the cases of CTNO (0.05)_600 and CTNO (0.1)_600, while an unknown weak peak was observed at $2\theta = 29.7^\circ$ in the case of CTNO (0.35)_600. It should be noted, however, that all the peaks at other positions were assignable to $\text{Cs}_{0.7}\text{Ti}_{1.825}\square_{0.175}\text{O}_4$ [21], indicating that the desired layered cesium titanate phase was obtained as the main phase in every case. Although we

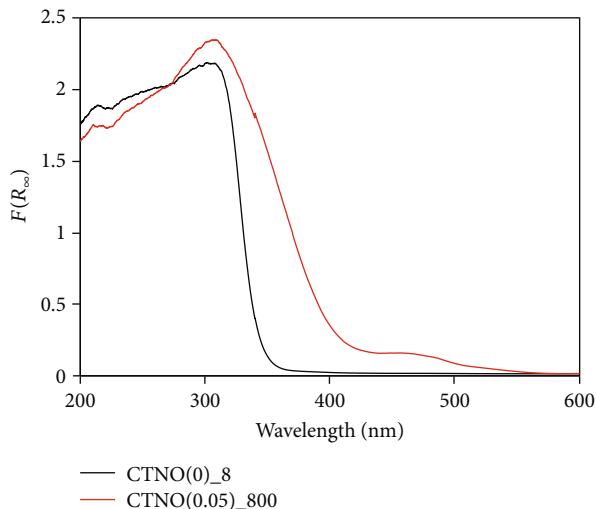


FIGURE 2: UV-vis DR spectra of CTNO (0)_800 and CTNO (0.05)_800.

anticipated that the XRD peaks would shift to smaller 2θ values due to doping in the octahedral site with Ni^{2+} with a larger ion radius (0.0690 nm) than that of Ti^{4+} (0.0605 nm) [29], no such shift was observed. As shown in Figure 4, the lattice constants of the Ni-doped samples were almost identical to that of CTNO (0)_600. This indicates that Ni-doping did not affect the crystal structure of CTNO (0)_600.

Figure 3(b) shows XRD patterns of HTNO (x)_600. XRD peaks assignable to $\text{H}_{0.7}\text{Ti}_{1.825}\square_{0.175}\text{O}_4$ and rutile were observed in all the samples, while that assignable to anatase was additionally observed in the case of $x = 0 - 0.1$. Given that no transformation occurred in CTNO (0.05)_800 after dilute HCl treatment and subsequent drying, it was apparent that a structural transformation of the Ni-doped layered cesium titanate into rutile as well as anatase was promoted by posttreatment when a sample prepared at a lower temperature was used as the starting material. The intensity of the peak at $2\theta = 10.2^\circ$ attributable to the (020) plane of $\text{H}_{0.7}\text{Ti}_{1.825}\square_{0.175}\text{O}_4$ increased with increases in the Ni content, while the intensity of the peak at $2\theta = 27.6^\circ$ attributable to the (110) plane of rutile decreased remarkably when the x value increased from 0.1 to 0.35. These results further confirm that the transformation of titanate sheets into rutile was suppressed by Ni-doping. The counter anion of the acids has been reported to affect the crystal phase of TiO_2 obtained from KTLO [22], and the structural transformation of KTLO into rutile by dilute HCl treatment and subsequent drying was explained by the effect of the chloride ion in the previous study [12]. In the present study, on the other hand, formation of anatase in addition to rutile was observed after posttreatment of CTNO (x)_600, except for the x value of 0.35. The composition of the starting material is likely to affect the TiO_2 phase transformed from titanate sheets, although the mechanism remains unclear.

Figure 5 displays Raman spectra of standard TiO_2 samples (anatase and rutile), HTNO (0.1)_600, and HTNO (0.35)_600. The Raman bands at 143, 394, 513, and 634 cm^{-1} of anatase were ascribable to the $E_g, A_{1g}, B_{1g},$ and E_g modes,

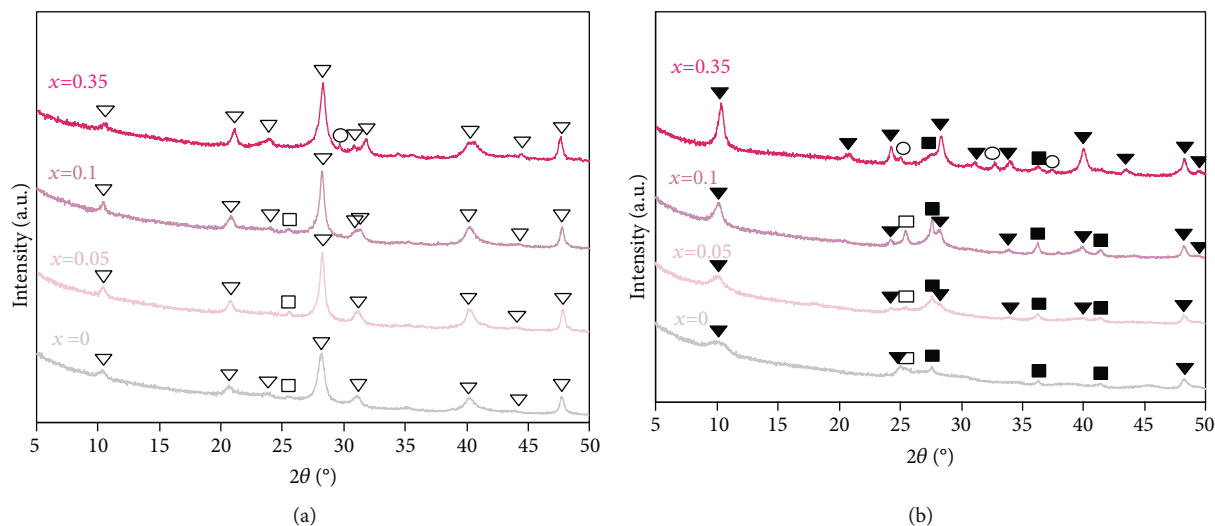


FIGURE 3: XRD patterns of (a) CTNO (x)₆₀₀ and (b) HTNO (x)₆₀₀: ∇ : $\text{Cs}_{0.7}\text{Ti}_{1.825}\square_{0.175}\text{O}_4$, \blacktriangledown : $\text{H}_{0.7}\text{Ti}_{1.825}\square_{0.175}\text{O}_4$, \square : TiO_2 (anatase), \blacksquare : TiO_2 (rutile), and \circ : unknown.

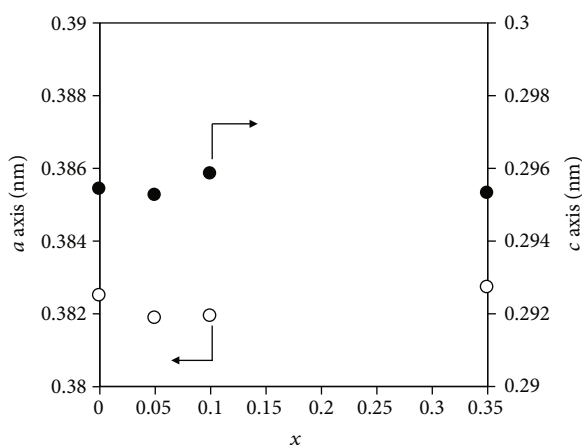


FIGURE 4: Lattice constant of CTNO (x)₆₀₀.

respectively, while those at 432 and 600 cm^{-1} of rutile were assigned to the E_g and A_{1g} modes, respectively [30]. In the case of HTNO (0.1)₆₀₀, the peaks at 136 cm^{-1} and 595 cm^{-1} were attributable to anatase and rutile, respectively, while the position of the band at 440 cm^{-1} was similar to that of the typical Raman band of $\text{H}_{0.7}\text{Ti}_{1.825}\square_{0.175}\text{O}_4$ (449 cm^{-1}) [31], further confirming that HTNO (0.1)₆₀₀ is a mixed phase of protonated layered titanate, anatase, and rutile. On the other hand, in the case of HTNO (0.35)₆₀₀, the Raman bands at 268 , 435 , and 710 cm^{-1} were attributable to $\text{H}_{0.7}\text{Ti}_{1.825}\square_{0.175}\text{O}_4$, while that at 594 cm^{-1} was attributable to rutile. The fact that no Raman bands attributable to anatase were observed correlates well with the results of the XRD analysis.

Figure 6(a) shows UV-vis DR spectra of CTNO (x)₆₀₀. The light absorption edge at a wavelength of 350 nm observed for CTNO (0)₆₀₀ shifted to longer wavelengths with increases in the Ni content. As shown in Table 1, the band gap energy of CTNO (0)₆₀₀ calculated by the Tauc plot [32] (Figure 6(b)) was 3.52 eV , which is slightly smaller

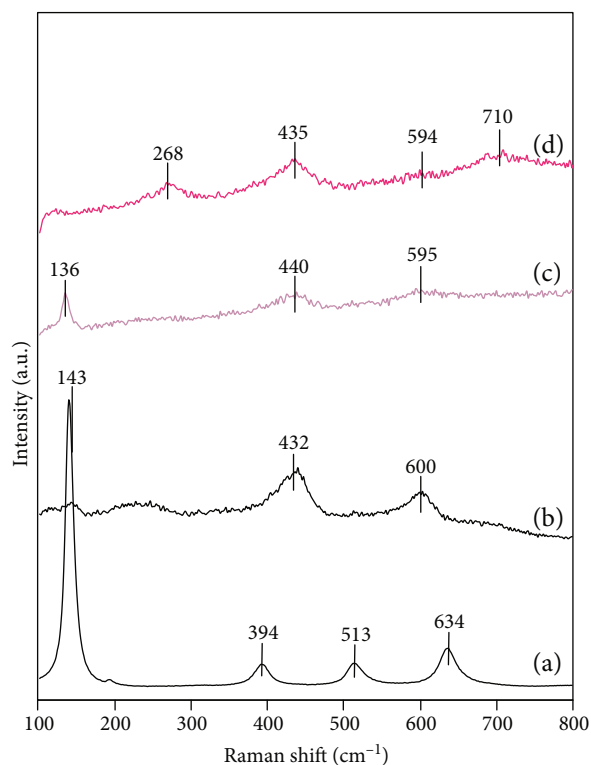


FIGURE 5: Raman spectra of (a) anatase (JRC-TIO-1), (b) rutile (JRC-TIO-16), (c) HTNO (0.1)₆₀₀, and (d) HTNO (0.35)₆₀₀.

than the value previously reported for layered cesium titanate (3.62 eV) whose composition ($\text{Cs}_{0.68}\text{Ti}_{1.83}\square_{0.17}\text{O}_4$) is similar to that of CTNO (0)₆₀₀ ($\text{Cs}_{0.7}\text{Ti}_{1.825}\square_{0.175}\text{O}_4$) [33]. The band gap energy decreased with increases in the Ni content. On the other hand, visible-light absorption at wavelengths shorter than 500 nm was introduced by Ni-doping, and the absorption increased with increases in the Ni content. The visible-light absorption changes are ascribable to the

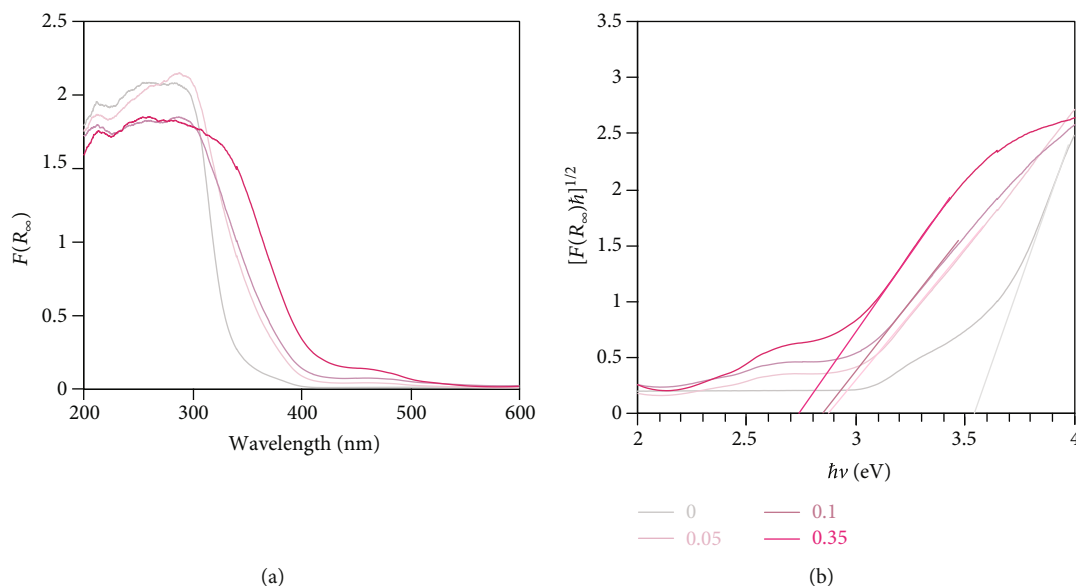


FIGURE 6: (a) UV-vis DR spectra and (b) Tauc plots of CTNO (x)₆₀₀; $x = 0, 0.05, 0.1, \text{ and } 0.35$.

TABLE 1: Band gap energies of different samples.

Sample	Band gap energy (eV)
CTNO (0) ₆₀₀	3.52
CTNO (0.05) ₆₀₀	2.88
CTNO (0.1) ₆₀₀	2.83
CTNO (0.35) ₆₀₀	2.73
HTNO (0) ₆₀₀	3.28
HTNO (0.05) ₆₀₀	3.08
HTNO (0.1) ₆₀₀	2.95
HTNO (0.35) ₆₀₀	2.81

introduction of localized energy states into the band gap by Ni-doping as mentioned above. As shown in Figure 7(a), the visible-light absorption attributable to the Ni-doping was observed in the samples even after dilute HCl treatment and subsequent drying, although the absorption intensity decreased, indicating that doped Ni was retained in the titanate sheets, whereas the majority of the doped Ni was extracted during dilute HCl treatment, as revealed by ICP-AES measurement (details to be presented later). As shown in the XPS spectrum of the Ni 2p region of HTNO (0.35)₆₀₀ (Figure 8), two peaks at 856.3 and 874.0 eV were observed, confirming the retention of Ni as a divalent form [34]. As shown in Table 1, the band gap energy of HTNO (0)₆₀₀ (3.28 eV) was smaller than that of CTNO (0)₆₀₀ (3.52 eV). A decreased band gap energy of a layered cesium titanate *via* interlayer protonation has previously been observed for $\text{Cs}_{0.68}\text{Ti}_{1.83}\text{O}_{0.17}\text{O}_4$ (3.62 to 3.47 eV) using dilute HCl treatment [33]. On the other hand, in the case of the Ni-doped samples, the band gap energy increased after dilute HCl treatment and subsequent drying. This correlates well with the blue shift of the light absorption edge of $\text{Cs}_{0.7}\text{Ti}_{1.65}\text{Ni}_{0.35}\text{O}_4$ after dilute HCl treatment in the previous report [20].

Table 2 shows the extraction rates of Ti and Ni from CTNO (x)₆₀₀ during dilute HCl treatment and the residual Ni/Ti ratios in the samples after dilute HCl treatment. While the Ni extraction rates were almost constant at 80-90%, those of Ti increased from 13.4 to 57.6% with increases in the Ni content. Accordingly, the residual Ni/Ti ratio in CTNO (x)₆₀₀ after dilute HCl treatment increased with increases in Ni content. The larger extraction rate for Ni compared with that reported for $\text{C}_{0.7}\text{Ti}_{1.65}\text{Ni}_{0.35}\text{O}_4$ under the same experimental conditions (0.5 M and 3 days for the HCl concentration and reaction time period, respectively) [20] was likely attributable to the smaller particle size of the sample in this study. This is because the preparation temperature of CTNO (x)₆₀₀ (600°C) in this study is lower than that of $\text{C}_{0.7}\text{Ti}_{1.65}\text{Ni}_{0.35}\text{O}_4$ in the previous report (800°C).

Figure 9 shows the photocatalytic NO conversion ratios over CTNO (x)₆₀₀ and HTNO (x)₆₀₀. Because the Ni-doped samples showed negligible photocatalytic activity under visible-light ($\lambda > 420 \text{ nm}$) irradiation in spite of their visible-light absorption properties, the photocatalytic performance of the samples was evaluated under irradiation by light with a wavelength longer than 290 nm. In the presence of water and oxygen, photooxidation was dominant for the mechanism of the NO_x decomposition reaction. The hydroxyl radical, $\cdot\text{OH}$, produced by photooxidation of H_2O , and the hydroperoxyl radical, $\cdot\text{OOH}$, generated by the reaction between H^+ and photoreduced oxygen (O^{2-}) were involved in the oxidation of NO to form HNO_3 [35–37]. Considering that water and oxygen were contained in the compressed air in the present study, NO was likely to have been decomposed by the photooxidation process. All the CTNO (x)₆₀₀ samples showed a NO conversion ratio approximately 1.8 times higher than P25, which is often used as a benchmark TiO_2 photocatalyst [38, 39]. The NO conversion ratio at CTNO (x)₆₀₀ was almost constant for all the Ni contents, indicating that the photocatalytic activity of CTNO (x)₆₀₀ was not dependent on the amount of doped Ni. After

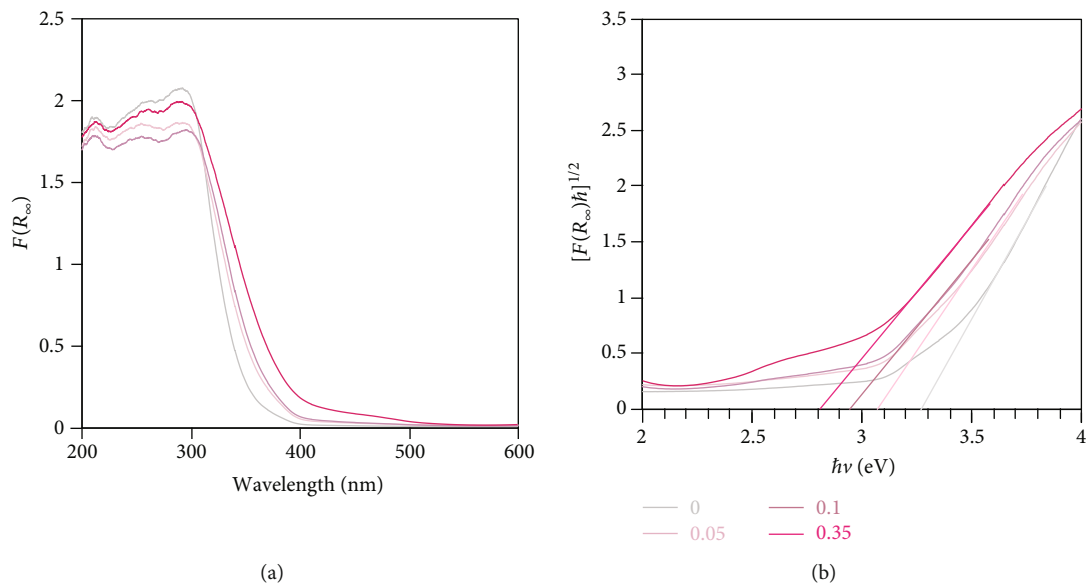
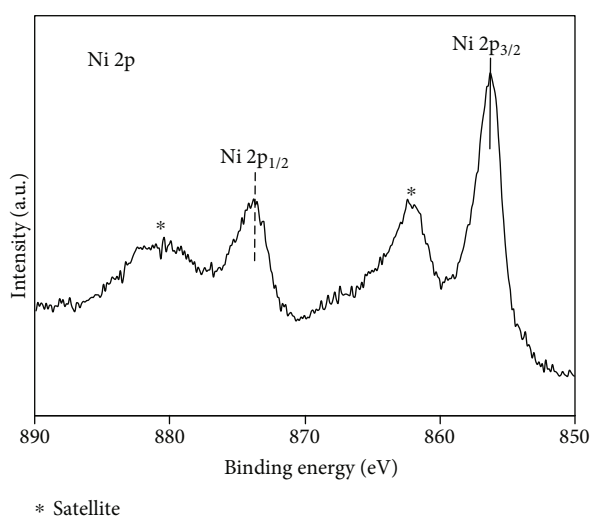


FIGURE 7: (a) UV-vis DR spectra and (b) Tauc plots of HTNO (x)₆₀₀, $x = 0, 0.05, 0.1,$ and 0.35 .



* Satellite

FIGURE 8: XPS spectrum of the Ni 2p region of HTNO (0.35)₆₀₀.

TABLE 2: Extraction rates of Ti and Ni and the corresponding residual Ni/Ti ratios in the CTNO (x)₆₀₀ samples after dilute HCl treatment.

Sample	Extraction rate		Residual Ni/Ti ratio
	Ni	Ti	
CTNO (0) ₆₀₀	N. D.	13.4	0
CTNO (0.05) ₆₀₀	84.1	24.9	5.9×10^{-3}
CTNO (0.1) ₆₀₀	89.5	55.3	13.2×10^{-3}
CTNO (0.35) ₆₀₀	80.5	57.6	97.6×10^{-3}

dilute HCl treatment and subsequent drying, the NO conversion ratio over CTNO (x)₆₀₀ decreased, except for the x value of 0.1, resulting in the highest NO conversion rate over HTNO (0.1)₆₀₀ among the HTNO (x)₆₀₀ samples. The photocat-

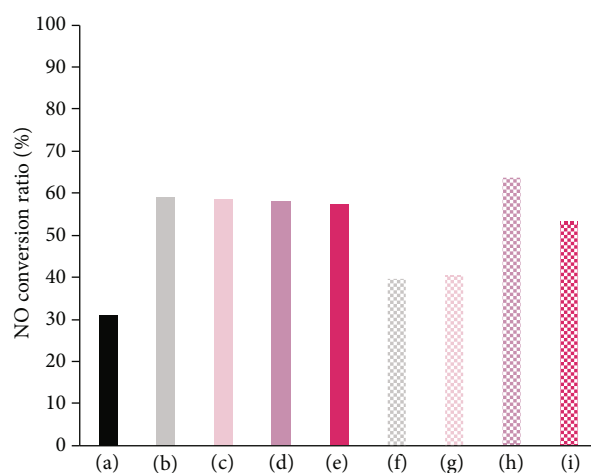


FIGURE 9: NO conversion ratios at (a) P25, CTNO (x)₆₀₀ with x values of (b) 0, (c) 0.05, (d) 0.1, and (e) 0.35, and HTNO (x)₆₀₀ with x values of (f) 0, (g) 0.05, (h) 0.1, and (i) 0.35.

lytic NO conversion rate over HTNO (0.1)₆₀₀ was twice as higher as that of P25. It should be noted that the design of a semiconductor photocatalyst for a NO_x decomposition reaction superior to that of P25 remains challenging [35] and that the activity of HTNO (0.1)₆₀₀ was comparable to that of a smart TiO_2 -based composite photocatalyst with excellent photocatalytic performance reported previously [40]. The best photocatalytic activity of HTNO (0.1)₆₀₀ among the HTNO (x)₆₀₀ samples was probably caused by a suitable ratio of protonated layered titanate and TiO_2 , because the interparticle charge transfer followed by enhanced photocatalytic activity depended largely on the phase composition of the TiO_2 -based composites [41–44]. As deduced from the XRD analyses, a layered titanate with low Ni content is likely to be transformed easily into TiO_2 (both anatase and rutile) to decrease the residual layered titanate phase. In light of the fact that the high photocatalytic

performance of the protonated layered titanate/rutile composite in the previous report was attributable to an electron transfer between two components [12], excess conversion of titanate sheets into TiO_2 to reduce the protonated layered titanate- TiO_2 interfaces is considered to be detrimental to photocatalytic performance. Accordingly, the photocatalytic activities of CTNO (0)_600 and CTNO (0.05)_600 decreased remarkably after dilute HCl treatment and subsequent drying. On the other hand, in the case of CTNO (0.35)_600, a relatively small decrease in the NO conversion ratio *via* dilute HCl treatment and the subsequent drying was attributable to the fact that the transformation of titanate sheets into TiO_2 was suppressed by Ni-doping, as mentioned above, and thus, almost no charge transfer occurred between the components. The mechanism of the improved photocatalytic activity of CTNO (0.1)_600 *via* posttreatment is possibly explained by the fact that the Ni-doped protonated layered titanate/ TiO_2 ratio was optimized to induce an efficient interparticle charge transfer and improve the charge separation efficiency. Also, doping with Ni can be effective for decreasing the number of Ti defect sites in layered titanate, which can induce charge recombination [45].

4. Conclusions

The lepidocrocite-type layered cesium titanate with nominal compositions of $\text{Cs}_{0.7}\text{Ti}_{1.825-x/2}\text{Ni}_x\text{O}_{0.175-x/2}\text{O}_4$ ($x = 0, 0.05, 0.1, \text{ and } 0.35$) was synthesized by solid-state reactions of Cs_2CO_3 , TiO_2 , and $\text{Ni}(\text{CH}_3\text{COO})_2 \cdot 4\text{H}_2\text{O}$ at different temperatures (600 or 800°C). The layered cesium titanate obtained by the solid-state reactions was treated with dilute HCl and subsequently dried to induce partial transformation into anatase- and rutile-type TiO_2 . When the solid-state reaction was conducted at 800°C, no structural transformation into TiO_2 was observed for the Ni-doped sample after posttreatment, while the sample obtained at 600°C was transformed into anatase and/or rutile for all the composition. The photocatalytic activity for the NO_x decomposition reaction of the samples obtained by the solid-state reaction at 600°C was not dependent on the doped Ni content. On the other hand, the layered cesium titanate with an x value of 0.1 after dilute HCl treatment and subsequent drying showed the highest photocatalytic activity among the samples, and the activity was twice as higher as that of P25, a benchmark photocatalyst for the reaction. This was likely attributable to the optimized Ni-doped protonated layered titanate/ TiO_2 phase ratio in the composite to induce an efficient interparticle electron transfer between these two components. Careful selection of the composition of the starting lepidocrocite-type layered titanate seems to be effective for designing layered titanate-based composite photocatalysts with improved photocatalytic performance.

Data Availability

The data used to support the findings of this paper are available from the corresponding author upon request.

Conflicts of Interest

The authors declare that they have no conflicts of interest.

Acknowledgments

This work was performed under the Cooperative Research Program of “Network Joint Research Center for Materials and Devices.”

References

- [1] Z. Wang, C. Li, and K. Domen, “Recent developments in heterogeneous photocatalysts for solar-driven overall water splitting,” *Chemical Society Reviews*, vol. 48, no. 7, pp. 2109–2125, 2019.
- [2] T. Ochiai and A. Fujishima, “Photoelectrochemical properties of TiO_2 photocatalyst and its applications for environmental purification,” *Journal of Photochemistry and Photobiology C: Photochemistry Reviews*, vol. 13, no. 4, pp. 247–262, 2012.
- [3] Y. Shiraishi and T. Hirai, “Selective organic transformations on titanium oxide-based photocatalysts,” *Journal of Photochemistry and Photobiology C: Photochemistry Reviews*, vol. 9, pp. 157–170, 2008.
- [4] P. Benjwal and K. K. Kar, “Simultaneous photocatalysis and adsorption based removal of inorganic and organic impurities from water by titania/activated carbon/carbonized epoxy nanocomposite,” *Journal of Environmental Chemical Engineering*, vol. 3, no. 3, pp. 2076–2083, 2015.
- [5] Y. K. Penke, A. K. Yadav, P. Sinha, I. Malik, J. Ramkumar, and K. K. Kar, “Arsenic remediation onto redox and photo-catalytic/electrocatalytic Mn-Al-Fe impregnated rGO: sustainable aspects of sludge as supercapacitor,” *Chemical Engineering Journal*, vol. 390, article 124000, 2020.
- [6] W. J. Youngblood, S.-H. A. Lee, K. Maeda, and T. E. Mallouk, “Visible light water splitting using dye-sensitized oxide semiconductors,” *Accounts of Chemical Research*, vol. 42, no. 12, pp. 1966–1973, 2009.
- [7] J. L. Gunjekar, I. Y. Kim, J. M. Lee, Y. K. Jo, and S. J. Hwang, “Exploration of nanostructured functional materials based on hybridization of inorganic 2D nanosheets,” *Journal of Physical Chemistry C: Nanomaterials and Interfaces*, vol. 118, no. 8, pp. 3847–3863, 2014.
- [8] D. Sangian, Y. Ide, Y. Bando, A. E. Rowan, and Y. Yamauchi, “Materials nanoarchitectonics using 2D layered materials: recent developments in the intercalation process,” *Small*, vol. 14, no. 33, article 1800551, 2018.
- [9] Y. Ide, Y. Nakasato, and M. Ogawa, “Molecular recognitive photocatalysis driven by the selective adsorption on layered titanates,” *Journal of American Chemical Society*, vol. 132, no. 10, pp. 3601–3604, 2010.
- [10] Y. Ide, M. Matsuoka, and M. Ogawa, “Efficient visible-light-induced photocatalytic activity on gold-nanoparticle-supported layered titanate,” *Journal of American Chemical Society*, vol. 132, pp. 16762–16764, 2010.
- [11] Y. Ide, M. Sadakane, T. Sano, and M. Ogawa, “Functionalization of layered titanates,” *Journal of Nanoscience and Nanotechnology*, vol. 14, no. 3, pp. 2135–2147, 2014.
- [12] K. Saito, S. Tominaka, S. Yoshihara, K. Ohara, Y. Sugahara, and Y. Ide, “Room-temperature rutile TiO_2 nanoparticle formation on protonated layered titanate for high-performance

- heterojunction creation," *ACS Applied Materials and Interfaces*, vol. 9, no. 29, pp. 24538–24544, 2017.
- [13] A. K. Yousef, M. Sanad, M. M. Rashad, A. A. El-Sayed, and Y. Ide, "Facile synthesis of layered titanate/rutile heterojunction photocatalysts," *Bulletin of the Chemical Society of Japan*, vol. 92, pp. 1801–1806, 2019.
- [14] J. Choi, H. Park, and M. R. Hoffmann, "Effects of single metal-ion doping on the visible-light photoreactivity of TiO₂," *Journal of Physical Chemistry C*, vol. 114, pp. 783–792, 2009.
- [15] L. Sun, J. Zhai, H. Li, Y. Zhao, H. Yang, and H. Yu, "Study of homologous elements: Fe, Co, and Ni dopant effects on the photoreactivity of TiO₂ nanosheets," *Chem Cat Chem*, vol. 6, pp. 339–347, 2014.
- [16] S. A. Ansari, M. M. Khan, M. O. Ansari, and M. H. Cho, "Nitrogen-doped titanium dioxide (N-doped TiO₂) for visible light photocatalysis," *New Journal of Chemistry*, vol. 40, no. 4, pp. 3000–3009, 2016.
- [17] P. Benjwal and K. K. Kar, "Removal of methylene blue from wastewater under a low power irradiation source by Zn, Mn co-doped TiO₂ photocatalysts," *RSC Advances*, vol. 5, pp. 98166–98176, 2015.
- [18] P. Benjwal and K. K. Kar, "One-step synthesis of Zn doped titania nanotubes and investigation of their visible photocatalytic activity," *Materials Chemistry and Physics*, vol. 160, pp. 279–288, 2015.
- [19] P. Benjwal, B. De, and K. K. Kar, "1-D and 2-D morphology of metal cation co-doped (Zn, Mn) TiO₂ and investigation of their photocatalytic activity," *Applied Surface Science*, vol. 427, pp. 262–272, 2018.
- [20] K. Saito, Y. Komiya, M. Sohmiya, M. Ogasawara, and S. Kato, "A phase separation in a protonated layered nickel titanate to form Ni-doped anatase/rutile TiO₂ nanocomposite with efficient visible-light responsive photocatalytic activity," *Journal of Asian Ceramic Societies*, vol. 8, no. 3, pp. 915–924, 2020.
- [21] T. Sasaki, M. Watanabe, Y. Michiue, Y. Komatsu, F. Izumi, and S. Takenouchi, "Preparation and acid-base properties of a protonated titanate with the lepidocrocite-like layer structure," *Chemistry of Materials*, vol. 7, pp. 1001–1007, 1995.
- [22] X. Yang, C. Karthik, X. Li et al., "Oriented nanocrystal arrays of selectable polymorphs by chemical sculpture," *Chemistry of Materials*, vol. 21, no. 14, pp. 3197–3201, 2009.
- [23] Y. Wang, L. Zhang, S. Li, and P. Jena, "Polyol-mediated synthesis of ultrafine TiO₂ nanocrystals and tailored physiochemical properties by Ni doping," *Journal of Physical Chemistry C*, vol. 113, no. 21, pp. 9210–9217, 2009.
- [24] Z. Zhou, M. Li, and L. Guo, "A first-principles theoretical simulation on the electronic structures and optical absorption properties for O vacancy and Ni impurity in TiO₂ photocatalysts," *Journal of Physical Chemistry Solids*, vol. 71, no. 12, pp. 1707–1712, 2010.
- [25] T. Sasaki, Y. Komatsu, and Y. Fujiki, "A new layered hydrous titanium dioxide H_xTi_{2-x/4}O₄·H₂O," *Journal of Chemical Society, Chemical Communication*, no. 12, pp. 817–818, 1991.
- [26] M. Hervieu and B. Raveau, "Structures en feuillets avec sites octaédriques lacunaires: les titanates non stoechiométriques Cs_{4x}Ti_{2-x}O₄," *Revue de Chimie Minérale*, vol. 18, pp. 642–649, 1981.
- [27] I. E. Grey, C. Li, I. C. Madsen, and J. A. Watts, "The stability and structure of," *Journal of Solid State Chemistry*, vol. 66, no. 1, pp. 7–19, 1987.
- [28] M. Ohashi, "Preparation and lithium intercalation of layer structured titanate Cs_xTi_{2-x/4}O₄ (x=0.68)," *Molecular Crystals and Liquid Crystals Science and Technology Section A Molecular Crystals and Liquid Crystals*, vol. 311, pp. 51–56, 2006.
- [29] R. D. Shannon, "Revised effective ionic radii and systematic studies of interatomic distances in halides and chalcogenides," *Acta Crystallographica*, vol. 32, no. 5, pp. 751–767, 1976.
- [30] U. Balachandran and N. G. Eror, "Raman spectra of titanium dioxide," *Journal of Solid State Chemistry*, vol. 42, no. 3, pp. 276–282, 1982.
- [31] T. Gao, H. Fjellvåg, and P. Norby, "Raman scattering properties of a protonic titanate H_xTi_{2-x/4}□_{x/4}O₄·H₂O (□, vacancy; x = 0.7) with lepidocrocite-type layered structure," *The Journal of Physical Chemistry. B*, vol. 112, no. 31, pp. 9400–9405, 2008.
- [32] J. Tauc, R. Grigorovici, and A. Vancu, "Optical properties and electronic structure of amorphous germanium," *Physica Status Solidi*, vol. 15, pp. 627–637, 1966.
- [33] G. Liu, L. Wang, C. Sun et al., "Band-to-band visible-light photon excitation and photoactivity induced by homogeneous nitrogen doping in layered titanates," *Chemistry of Materials*, vol. 21, pp. 1266–1274, 2009.
- [34] K. Fan, H. Chen, Y. Ji et al., "Nickel-vanadium monolayer double hydroxide for efficient electrochemical water oxidation," *Nature communications*, vol. 7, no. 1, 2016.
- [35] S. Yin, D. I. Maeda, and M. Wu, "Synthesis of HTaWO₆/(Pt, TiO₂) nanocomposite with high photocatalytic activities for hydrogen evolution and nitrogen monoxide destruction," *Solid State Ionics*, vol. 151, no. 1–4, pp. 377–383, 2002.
- [36] Y. Asakura, Y. Inaguma, K. Ueda, Y. Masubuchi, and S. Yin, "Synthesis of gallium oxynitride nanoparticles through hydrothermal reaction in the presence of acetylene black and their photocatalytic NO_x decomposition," *Nanoscale*, vol. 10, no. 4, pp. 1837–1844, 2018.
- [37] J. Wang, Y. Asakura, and S. Yin, "Synthesis of zinc germanium oxynitride nanotube as a visible-light driven photocatalyst for NO_x decomposition through ordered morphological transformation from Zn₂GeO₄ nanorod obtained by hydrothermal reaction," *Journal of Hazardous Materials*, vol. 396, p. 122709, 2020.
- [38] R. I. Bickley, T. Gonzalez-Carreno, J. S. Lees, L. Palmisano, and R. J. Tilley, "A structural investigation of titanium dioxide photocatalyst," *Journal of Solid State Chemistry*, vol. 92, pp. 178–190, 1991.
- [39] T. Ohno, K. Sarukawa, K. Tokieda, and M. Matsumura, "Morphology of a TiO₂ photocatalyst (Degussa, P-25) consisting of anatase and rutile crystalline phases," *Journal of Catalysis*, vol. 203, no. 1, pp. 82–86, 2001.
- [40] Y. Wei, Y. Huang, J. Wu et al., "Synthesis of hierarchically structured ZnO spheres by facile methods and their photocatalytic deNO_x properties," *Journal of Hazardous Materials*, vol. 248–249, pp. 202–210, 2013.
- [41] J. Zhang, Q. Xu, Z. Feng, M. Li, and C. Li, "Importance of the relationship between surface phases and photocatalytic activity of TiO₂," *Angewandte Chemie International Edition*, vol. 47, no. 9, pp. 1766–1769, 2008.
- [42] H. Xu and L. Zhang, "Controllable one-pot synthesis and enhanced photocatalytic activity of mixed-phase TiO₂ nanocrystals with tunable brookite/rutile ratios," *Journal of Physical Chemistry C*, vol. 113, no. 5, pp. 1785–1790, 2009.

- [43] R. Su, R. Bechstein, L. SØ et al., "How the anatase-to-rutile ratio influences the photoreactivity of TiO_2 ," *The Journal of Physical Chemistry C*, vol. 115, no. 49, pp. 24287–24292, 2011.
- [44] L. Cao, D. Chen, W. Li, and R. A. Caruso, "Hierarchically porous titania networks with tunable anatase: rutile ratios and their enhanced photocatalytic activities," *ACS Applied Materials and Interfaces*, vol. 6, no. 15, pp. 13129–13137, 2014.
- [45] K. Saito, E. Yi, R. M. Laine, and Y. Sugahara, "Preparation of Nb-doped TiO_2 nanopowder by liquid-feed spray pyrolysis followed by ammonia annealing for tunable visible-light absorption and inhibition of photocatalytic activity," *Ceramics International*, vol. 46, no. 2, pp. 1314–1322, 2020.

Research Article

Guest-Host Interactions in Symmetrical Carboxy Heptamethine Cyanine Dyes-Titanium Dioxide Systems: Synthesis, Theoretical Calculations, Aggregation Properties, and Application in Dye-Sensitized Solar Cells

Rodrigo da Costa Duarte ¹, Matheus Costa de Oliveira,² Josene Maria Toldo ^{3,4},
Paulo Fernando Bruno Gonçalves ³, Marcos José Leite Santos ²,
and Fabiano Severo Rodembusch ¹

¹Grupo de Pesquisa em Fotoquímica Orgânica Aplicada (GPFOA), Instituto de Química, Universidade Federal do Rio Grande do Sul, Av. Bento Gonçalves 9500 CEP 91501-970 Porto Alegre RS, Brazil

²Laboratório de Materiais Aplicados e Interfaces (LAMAI), Instituto de Química, Universidade Federal do Rio Grande do Sul, Av. Bento Gonçalves 9500 CEP 91501-970 Porto Alegre RS, Brazil

³Grupo de Química Teórica e Computacional, Universidade Federal do Rio Grande do Sul-Instituto de Química, Avenida Bento Gonçalves, 9500, CP 15003, CEP 91501-970 Porto Alegre RS, Brazil

⁴Aix Marseille University, CNRS, ICR, Marseille, France

Correspondence should be addressed to Marcos José Leite Santos; mjls@ufrgs.br
and Fabiano Severo Rodembusch; rodembusch@iq.ufrgs.br

Received 11 September 2020; Revised 8 December 2020; Accepted 9 January 2021; Published 27 January 2021

Academic Editor: Takuya Fujimura

Copyright © 2021 Rodrigo da Costa Duarte et al. This is an open access article distributed under the Creative Commons Attribution License, which permits unrestricted use, distribution, and reproduction in any medium, provided the original work is properly cited.

In this work, the role of deoxycholic acid (DCA) as a coadsorbent was investigated in the sensitization of mesoporous TiO₂ layers (host) with symmetrical carboxy heptamethine cyanine dyes (guest). Different approaches have been tested, aimed at reducing the H-aggregation and minimizing the competition between cyanine molecules and DCA for active sites of the host, thus improving solar cell efficiency. Heptamethine cyanines containing carboxylic anchoring groups were obtained with good yields. The cyanines present UV-Vis absorption in methanol and dimethylformamide solutions ascribed to fully allowed electronic transitions (¹ππ*), as well as fluorescence emission in the NIR region, with any evidence of aggregations in both ground and excited states. TD-DFT calculations were also performed in order to study the geometry and charge distribution of these compounds in their ground and excited electronic states. Solid-state photophysics indicates that the cyanines showed excellent adsorption on TiO₂, which can be justified by the presence of the -COOH moieties in the structure. Photophysical measurements have revealed the best concentrations of dye and DCA, which resulted in efficient inhibition of cyanine H-aggregates on the TiO₂ surface in addition to allow large dye loading. HOMO and LUMO energy levels of the dyes were identified by cyclic voltammetry, showing oxidation and reduction potentials within acceptable limits for application as a photosensitizer in dye-sensitized solar cells (DSSCs) based on a TiO₂ mesoporous photoanode. Assembled DSSCs have shown a large improvement of the electrical parameters and efficiency when a balance between dye aggregation and the competition to the host active sites was reached.

1. Introduction

Heptamethine cyanines are organic cationic or neutral compounds, structurally constituted by two heterocyclic nitrogenous portions interconnected by a polymetallic chain [1]. This structural configuration gives these compounds bands of absorption and fluorescence emission that vary from 700 to 1000 nm and can be modulated according to the number of vinyl groups present in the unsaturated chain [1]. Due to their photophysical properties in the near-infrared, this class of dyes has been explored in many technological applications, such as in hybrid solar cells [2] and nonlinear absorbing materials [3, 4], and in bioanalysis, such as enzymatic assays, immunoassays, cancer detection, diagnosis modalities, identification of metallic ions, and pH studies, and as a drug carrier [5–10]. Yet, special attention has been given to heptamethine cyanines in dye-sensitized solar cell applications [11–17]. These metal-free sensitizers can present some advantages over ruthenium-based complexes, commonly used for sensitization: they are much cheaper and have higher molar extinction coefficients, in addition to present absorption at longer wavelengths [18], and their molecular design—and consequently their obtention—can be easily customized. Nevertheless, the well-known easy formation of aggregates in heptamethine cyanines [19, 20] is a major drawback in the particular for applications in DSSC, resulting in decreased solar cell performance [2, 21].

To reduce the formation of aggregates on the photoanode, some compounds known as coadsorbents can be applied as additives in the sensitizing dye solution [2, 21], such as chenodeoxycholic acid (CDCA) and deoxycholic acid (DCA). Previous works have shown that a lower concentration of the coadsorbent already plays a significant role in solar cell efficiency, while by increasing the concentration, the contribution of H-aggregates is reduced and the solar cell efficiency increases [20, 22]. In the case of heptamethine cyanines (guest) adsorbed on TiO₂ mesoporous film (host), as presented by Ziólek et al., the gain in efficiency can be explained by taking the excited state dynamics of the components into account.

In this paper, we study the effect of aggregation of heptamethine cyanine symmetrical dyes (guest) on TiO₂ nanoparticles (host), applying deoxycholic acid (DCA) as a coadsorbent to evaluate the suppression capacity of the dye aggregation. Also, the experimental and theoretical photophysical characterizations of these compounds are presented and discussed, and sensitized solar cells were assembled with an optimized dye: coadsorbent ratio.

2. Experimental

2.1. Material and Methods. *p*-Aminobenzoic acid, 3-methyl-2-butanone, sodium acetate, and SnCl₂·2H₂O were purchased from Sigma-Aldrich. NaNO₂, HCl, MeOH, and CH₃COOH were acquired from Synth. POCl₃ and iodomethane were acquired from Sigma. 4-Methylcyclohexanone, 4-ethylcyclohexanone, and 4-tert-butylcyclohexanone were acquired from Alfa Aesar. Thin layer chromatography was performed using Silica Gel 60 F254. Column chromatog-

raphy was performed using Silica Gel 60 Å (70–230 mesh). Infrared spectra were obtained with a Shimadzu-IR PRESTIGE-21 spectrometer in the NaCl window. The acquisition was made at room temperature with 20 scans and 4.0 cm⁻¹ resolution. ¹H and ¹³C NMR analyses were performed with a Bruker Scientific apparatus operating at 400 MHz for ¹H and 100 MHz for ¹³C or a Varian VNMRs 300 MHz spectrometer operating at 300 MHz for ¹H and 75 MHz for ¹³C using deuterated dimethylsulfoxide (DMSO-*d*₆) or chloroform (CDCl₃). Chemical shifts (δ) were measured in ppm, and coupling constants (*J*) in Hz. ¹H NMR spectra were expressed regarding their multiplicity (*s*, singlet; *d*, doublet; *m*, multiplet), coupling constant, and relative number of hydrogens. UV-Vis absorption spectra were obtained with a Shimadzu UV-2450 spectrophotometer in a 10⁻⁶ M solution at a spectral resolution of 0.1 nm. Solid-state measurements were obtained on a Shimadzu UV-2450 spectrophotometer using an ISR-2200 Integrating Sphere Attachment. The baseline was obtained using BaSO₄ (Wako Pure Chemical Industries, Ltd.). In these experiments, the samples were treated as powder. All measurements were carried out at 25°C. Steady-state fluorescence spectra were obtained using a Shimadzu RF-5301PC spectrofluorometer. The maximum absorption wavelength was set as the excitation radiation for emission measurements. Cyclic voltammetry (CV) was performed on a PalmSens3 potentiostat/galvanostat, using a solution of tetra-*N*-butylammonium hexafluorophosphate (TBAPF₆) in CH₂Cl₂ (0.1 M) as the supporting electrolyte. A three-electrode cell was used comprised of a glassy carbon electrode as the working electrode, a platinum wire as the counter electrode, and an Ag/Ag⁺ reference electrode. The cell was deoxygenated by purging with argon before each measurement. Ferrocene/ferricenium (Fc/Fc⁺) redox couple was used as the internal reference. The performance of the DSSCs was evaluated by current versus potential measurements, carried out using a 300 W xenon arc lamp and an AM1.5 filter. The power of the simulated light was calibrated to 100 mW·cm⁻² and recorded by a picoamperimeter Keithley, model 2400.

2.2. Synthesis

2.2.1. 2,3,3-Trimethyl-3H-indole-5-carboxylic Acid (3). In a round-bottom flask were added 4-hydrazinylbenzoic acid (1) (1.0 g, 6.5 mmol), 3-methylbutan-2-one (2) (2.8 g, 32 mmol), and 40 ml of glacial acetic acid, and the reaction was maintained under reflux for 12 h. After this period, the reaction mixture was concentrated under vacuum, and dichloromethane (50 ml) was added to the flask. Then, this solution was treated with NaHCO₃ saturated solution (1 × 50 ml). The aqueous phase was extracted with dichloromethane (2 × 50 ml). The combined organic layers were dried using MgSO₄ and concentrated under vacuum. The product was obtained in 58% yield and used in the next step without purification.

Red solid: yield: 58%. ¹H NMR (CDCl₃, 300 MHz): δ (ppm) 10.54 (s, 1H, *J* = 8.0 Hz), 8.16 (d, 1H, *J* = 9.0 Hz), 8.09 (s, 1H), 7.70 (d, 1H, *J* = 9.0 Hz), 2.41 (s, 3H), and 1.38 (s, 6H). ¹³C NMR (CDCl₃, 75 MHz): δ (ppm) 192.7, 171.0, 157.0, 145.5, 130.9, 127.5, 123.3, 119.7, 54.0, 23.0, and 15.6.

2.2.2. *5-Carboxy-1,2,3,3-tetramethyl-3H-indol-1-ium (5)*. In a round-bottom flask were added 3 (0.50 g, 2.4 mmol), iodo-methane (4) (1.70 g, 12 mmol), and acetonitrile (20 ml). The reaction was maintained under 56°C for 12 h. After this period, ethyl acetate (40 ml) was added, and the mixture was cooled at room temperature and maintained under agitation for 30 min. Then, the resulting solid was filtered and dried under vacuum. The product was obtained in 65% of yield and used in the next step without purification.

Pink solid: yield: 65%. M.p.: 251-253°C. ¹H NMR (CDCl₃, 400 MHz): δ (ppm) 8.36 (s, 1H), 8.17 (d, 1H, *J* = 9.0 Hz), 8.03 (d, 1H, *J* = 9.0 Hz), 4.01 (s, 3H), 2.84 (s, 3H), and 1.57 (s, 6H). ¹³C NMR (CDCl₃, 100 MHz): δ (ppm) 199.4, 166.9, 145.7, 142.3, 131.9, 130.7, 124.6, 115.8, 54.7, 35.6, 21.9, and 15.2.

2.2.3. *Pentamethinic Salts (11a-c)*. In a round-bottom flask cooled to 0° C, 2.4 ml of DMF (2.26 g, 31 mmol) and 2 ml of POCl₃ (3.37 g, 22mmol) were added dropwise, and this mixture was stirred for 30 minutes. After 1.13 ml of cyclohexanone 6 (1.07 g, 9.6 mmol) was added, the reaction mixture was kept under stirring and reflux for 2 h. After this period, the reaction temperature was reduced to room temperature and a mixture of aniline (10) and ethanol [1:1 (v/v), 3.3 ml] was added and kept under stirring for 1 h. After this period, the reaction crude was poured into a mixture of ice and concentrated HCl (10:1, 20 ml) for 12 h. After this period, the resulting solid was filtered and washed as H₂O, recrystallized from toluene, filtered with filter paper, and dried under vacuum. A similar procedure was performed for obtaining the compounds 11b and 11c using cyclohexanones 7 and 8, respectively.

N-((E)-((E)-2-Chloro-5-methyl-3-((phenylamino)methylene)cyclohex-1-en-1-yl)methylene)benzenaminium chloride (11a): violet solid. Yield: 70% (2.50 g). M.p.: 221°C. FTIR (cm⁻¹): 3042, 2946, 2868, 1607, 1565, 1465, and 1297. ¹H NMR (DMSO-*d*₆, 400 MHz): δ (ppm) 11.22 (s, 2H), 8.53 (s, 2H), 7.58 (m, 4H), 7.44 (m, 4H), 7.25 (m, 2H), 3.02 (m, 2H), 2.22 (m, 2H), 1.92 (m, 1H), and 1.14 (d, 3H, *J* = 4.0 Hz).

N-((E)-((E)-2-Chloro-5-ethyl-3-((phenylamino)methylene)cyclohex-1-en-1-yl)methylene)benzenaminium chloride (11b): violet solid. Yield: 58% (2.15 g). M.p.: 219-222°C. FTIR (cm⁻¹): 3090, 2958, 2855, 1607, 1565, 1453, and 1261. ¹H NMR (DMSO-*d*₆, 300 MHz): δ (ppm) 11.34 (s, 2H), 8.51 (s, 2H), 7.60 (m, 4H), 7.44 (m, 4H), 7.25 (m, 2H), 3.09 (m, 2H), 2.18 (m, 2H), 1.65 (m, 1H), 1.47 (q, 2H, *J* = 7.2 Hz), and 1.05 (t, 3H, *J* = 7.2 Hz).

N-((E)-((E)-5-(tert-Butyl)-2-chloro-3-((phenylamino)methylene)cyclohex-1-en-1-yl)methylene)benzenaminium chloride (11c): violet solid. Yield: 75% (2.99 g). M.p.: 217-219°C; FTIR (cm⁻¹): 3060, 2952, 2874, 1607, 1571, 1469, and 1267. ¹H NMR (DMSO-*d*₆, 400 MHz): δ (ppm) 11.40 (s, 2H), 8.52 (s, 2H), 7.58 (m, 4H), 7.46 (m, 4H), 7.27 (m, 2H), 3.06 (m, 2H), 2.14 (m, 2H), 1.47 (m, 1H), and 1.05 (m, 9H).

2.2.4. *Carboxy Heptamethine Cyanines (12-14)*. In a round-bottomed monotubulated amber flask, 20 ml of isopropanol was added and subsequently closed with a septum. Then, N₂ was bubbled through the isopropanol for 15 min. After bubbling with nitrogen, compound 11a (0.18 g, 0.5 mmol),

CH₃COONa (0.12 g 1.5 mmol), and indole 5 (0.51 g 1.5 mmol) were added. The reaction mixture was kept at reflux, under N₂ atmosphere for 18 h. At the end of the reaction, the solvent was evaporated under reduced pressure. The obtained solid was purified by washing with 150 ml of dichloromethane, carried out in an ultrasound bath for 30 min. After 12 hours, this washing process was repeated 4 times. The obtained solid was filtered through filter paper and washed with 40 ml distilled water followed by 15 ml ethyl ether. Then, the obtained solid was filtered through filter paper and dried under vacuum. A similar procedure was performed for obtaining the compounds 13 and 14 using the intermediates 11b and 11c, respectively.

5-Carboxy-2-((E)-2-((E)-3-(2-((E)-5-carboxy-1,3,3-trimethylindolin-2-ylidene)ethylidene)-2-chloro-5-methylcyclohex-1-en-1-yl)vinyl)-1,3,3-trimethyl-3H-indol-1-ium iodide (12): green solid. Yield: 52% (0.18 g). M.p.: 257-259°C. FTIR (cm⁻¹): 3423, 3052, 2966, 2878, 1704, and 1548. ¹H NMR (DMSO-*d*₆, 400 MHz): δ (ppm) 8.27 (d, 2H, *J* = 16.0 Hz), 8.14 (s, 1H), 8.02 (d, 2H, *J* = 12.0 Hz), 7.52 (d, 2H, *J* = 12.0 Hz), 6.37 (d, 2H, *J* = 12.0 Hz), 3.71 (s, 6H), 2.96 (m, 2H), 2.20 (m, 2H), 1.93 (m, 1H), and 1.69 (s, 12H), 1.16 (d, 3H, *J* = 8.0 Hz). ¹³C NMR (DMSO-*d*₆, 100 MHz): δ (ppm) 173.9, 167.3, 148.9, 146.9, 143.8, 141.6, 131.0, 127.7, 127.6, 123.7, 111.7, 103.5, 49.1, 34.0, 32.4, 27.7, 27.6, and 21.3.

5-Carboxy-2-((E)-2-((E)-3-(2-((E)-5-carboxy-1,3,3-trimethylindolin-2-ylidene)ethylidene)-2-chloro-5-ethylcyclohex-1-en-1-yl)vinyl)-1,3,3-trimethyl-3H-indol-1-ium iodide (13): green solid. Yield: 57% (0.20 g). M.p.: 251-254°C. FTIR (cm⁻¹): 3423, 3052, 2966, 2869, 1704, and 1557. ¹H NMR (DMSO-*d*₆, 400 MHz): δ (ppm) 8.27 (d, 2H, *J* = 12.0 Hz), 8.13 (s, 1H), 8.01 (d, 2H, *J* = 8.0 Hz), 7.51 (d, 2H, *J* = 8.0 Hz), 6.39 (d, 2H, *J* = 12.0 Hz), 3.71 (s, 6H), 2.97 (m, 2H), 2.21 (m, 2H), 1.68 (s, 12H), 1.49 (m, 2H), and 1.04 (t, 3H, *J* = 8.0 Hz). ¹³C NMR (DMSO-*d*₆, 100 MHz): δ (ppm) 173.9, 167.3, 149.0, 146.9, 143.9, 141.6, 131.0, 127.7, 127.6, 123.7, 111.7, 103.4, 49.1, 33.8, 32.3, 31.9, 28.2, 27.6 (2C), and 11.9.

2-((E)-2-((E)-5-(tert-Butyl)-3-(2-((E)-5-carboxy-1,3,3-trimethylindolin-2-ylidene)ethylidene)-2-chlorocyclohex-1-en-1-yl)vinyl)-5-carboxy-1,3,3-trimethyl-3H-indol-1-ium iodide (14): green solid. Yield: 53% (0.20 g). M.p.: 260-265°C. FTIR (cm⁻¹): 3432, 3034, 2966, 2878, 1695, and 1557. ¹H NMR (DMSO-*d*₆, 400 MHz): δ (ppm) 8.28 (d, 2H, *J* = 12.0 Hz), 8.12 (s, 1H), 8.01 (d, 2H, *J* = 12.0 Hz), 7.50 (d, 2H, *J* = 6.0 Hz), 6.39 (d, 2H, *J* = 12.0 Hz), 3.72 (s, 6H), 2.96 (m, 2H), 2.19 (m, 2H), 1.69 (s, 12H), 1.49 (m, 1H), and 1.05 (s, 9H). ¹³C NMR (DMSO-*d*₆, 100 MHz): δ (ppm) 173.9, 167.3, 149.0, 146.9, 143.9, 141.6, 131.0, 128.4, 127.5, 123.7, 111.7, 103.2, 49.2, 32.7, 32.3, 29.9, 27.7, and 27.6.

2.3. *Theoretical Calculations*. Theoretical calculations were done using Density Functional Theory (DFT) and Time-Dependent Density Functional Theory (TD-DFT) with Gaussian 16 RevA.03 [23] program. The structures of the ground (S₀) and first excited singlet (S₁) states were optimized using the M06-2X functional [24] and 6-31G(d,p) basis set [25]. This functional was selected after a benchmarking against the experimental values of absorption and emission maxima wavelengths. Yet, previous works have

TABLE 1: Experimental conditions for the study of coadsorption of deoxycholic acid (DCA) and cyanine 13 as a model in methanol solutions on TiO₂ mesoporous layer.

Methodology	Type	Conditions
#1	One-step adsorption	Dye concentration: 5.0 mM; DCA concentrations: 2, 6, 20, and 40 mM; TiO ₂ temperature: 80°C; adsorption time: 24 h
#2		Dye concentration: 5.0 mM; DCA concentrations: 2, 6, 20, and 40 mM; TiO ₂ temperature: 22°C; adsorption time: 24 h
#3		Dye concentration: 5.0 mM; DCA concentrations: 2, 6, 20, and 40 mM; TiO ₂ temperature: 22°C; adsorption time: 1 h
#4		Dye concentration: 0.1 mM. DCA concentrations: 2, 6, and 20 mM; TiO ₂ temperature: 22°C; adsorption time: 1 h
#5	Two-step adsorption	First step: DCA concentrations—2, 6, and 20 mM; Second step: dye concentration—0.1 mM; TiO ₂ temperature: 22°C; adsorption time: 1 h

pointed out the efficiency of hybrid functionals with ~50% of the Hartree-Fock exchange to simulate the electronic spectra of cyanine dyes, with average errors of 0.29 eV for the M06-2X functional [26–28]. The minimum energies structures were verified by vibrational analysis. Vertical absorption and emission energies were computed at the M06-2X/6-311+G(d,p) level of theory. The solvent effects were included by applying the integral equation formalism of the polarizable continuum model (IEF-PCM) [29–31] using methanol and *N,N*-dimethylformamide (DMF) as solvents. To analyze the character of the excitations, natural transition orbitals (NTOs) [32] were obtained at the same level of theory using the Gaussian 16 program. For insights on the power conversion efficiency of DSSC devices, we also calculated the HOMO-LUMO band gaps, ESP (electrostatic surface potential) analysis using charges derived from potential (ChelpG), and light harvesting efficiency (LHE) from DFT/TD-DFT calculations.

2.4. DSSC Preparation. The TiO₂ paste was screenprinted on the transparent conductive substrate (fluorine-doped tin oxide, FTO) previously soaked in a 40 mM TiCl₄ aqueous solution at 60°C for 30 minutes. The substrate was heated on a hot plate at 125°C for 20 min and at 450°C for 30 min in a tubular oven. The mesoporous TiO₂ electrode was immersed in 0.1 mM of 13 and kept at room temperature 24 h (see Section 2.6). The counterelectrodes were prepared by coating the FTO surface with 30 μl of 1 mM hexachloroplatinic acid and heated at 500°C. The mediator, responsible for the regeneration of the dye, was placed in between the dye-sensitized photoanode and the counterelectrode. The device was sealed using a polymeric film of low melting temperature (Meltonix). The electrolyte was a 0.6 M BMII, 0.03 M I₂, 0.10 M guanidinium thiocyanate, and 4-tertbutylpyridine (0.5 M) in a mixture of acetonitrile and valeronitrile. Additional information for the anode and cathode preparation can be found as supplementary material.

2.5. Coadsorption Study. Five different methodologies of adsorption on the mesoporous TiO₂ films were proposed and evaluated (1-5) using compound 13 as a model (Table 1). In this study, the aggregation effect was evaluated taking the intensity of the H-aggregate absorption band located at around 700 nm into account (Figure 1).

2.6. Electrical Characterization of the Assembled Devices. Electrical current versus electrical potential curves (*I* – *V*) were acquired within the range of -0.2 V to +1.1 V with seventeen different voltage levels (mean interval of 75 mV) to characterize the DSSCs. The experiments were carried out using a xenon lamp of 300 W, with an incident light intensity of 100 mW·cm⁻², fed by a source model 66485 using a filter AM1.5 and a picoammeter Keithley model 2410-c. Light intensity was measured by using a photodiode model 71648-71608.

3. Results and Discussion

3.1. Synthesis. The carboxy heptamethine cyanine dyes 12-14 were prepared as presented in Scheme 1. The heterocyclic compound 3 was prepared according to the literature [33]. Initially, 4-hydrazinobenzoic acid (1) reacted with 3-methylbutan-2-one (2) under reflux to obtain the intermediate compound 2,3,3-trimethyl-3*H*-indole-5-carboxylic acid (3) by Fischer cyclization [34]. Then, 3 was alkylated with iodomethane (4) in a nitrogen atmosphere to obtain the quaternized indole 5.

Pentamethinic salts 11a-c were synthesized from an adapted methodology already described in the literature [35]. The methodology consists of two steps, employing a formylating system containing the respective hexanones 6-8 and POCl₃/DMF/PhNH₃⁺Cl⁻. In the first step, there is the formation of the Vilsmeier-Haack reagent through the slow addition of POCl₃ in DMF under an ice bath, which generated a reddish solution evidencing the formation of chlorine ion. Then, the respective cyclohexanone was added under an ice bath. In the second step, an alcoholic solution of aniline was added to the reaction mixture at room temperature and left under stirring in an acidic medium. The compounds 11a-c were obtained with crude yields between 58 and 75%.

The synthetic method for obtaining the desired compounds 12-14 occurs similar to the Knoevenagel condensation, but in this case, the condensation reactions take place between the bis iminic pentamethine salts 11a-c with compound 5 using sodium acetate as the base and isopropyl alcohol (HPLC grade) as the solvent under reflux (Scheme 1). To minimize the photooxidation processes that can be prejudicial to the stability of these structures [36], the synthesis was performed in the dark with the use of amber glassware

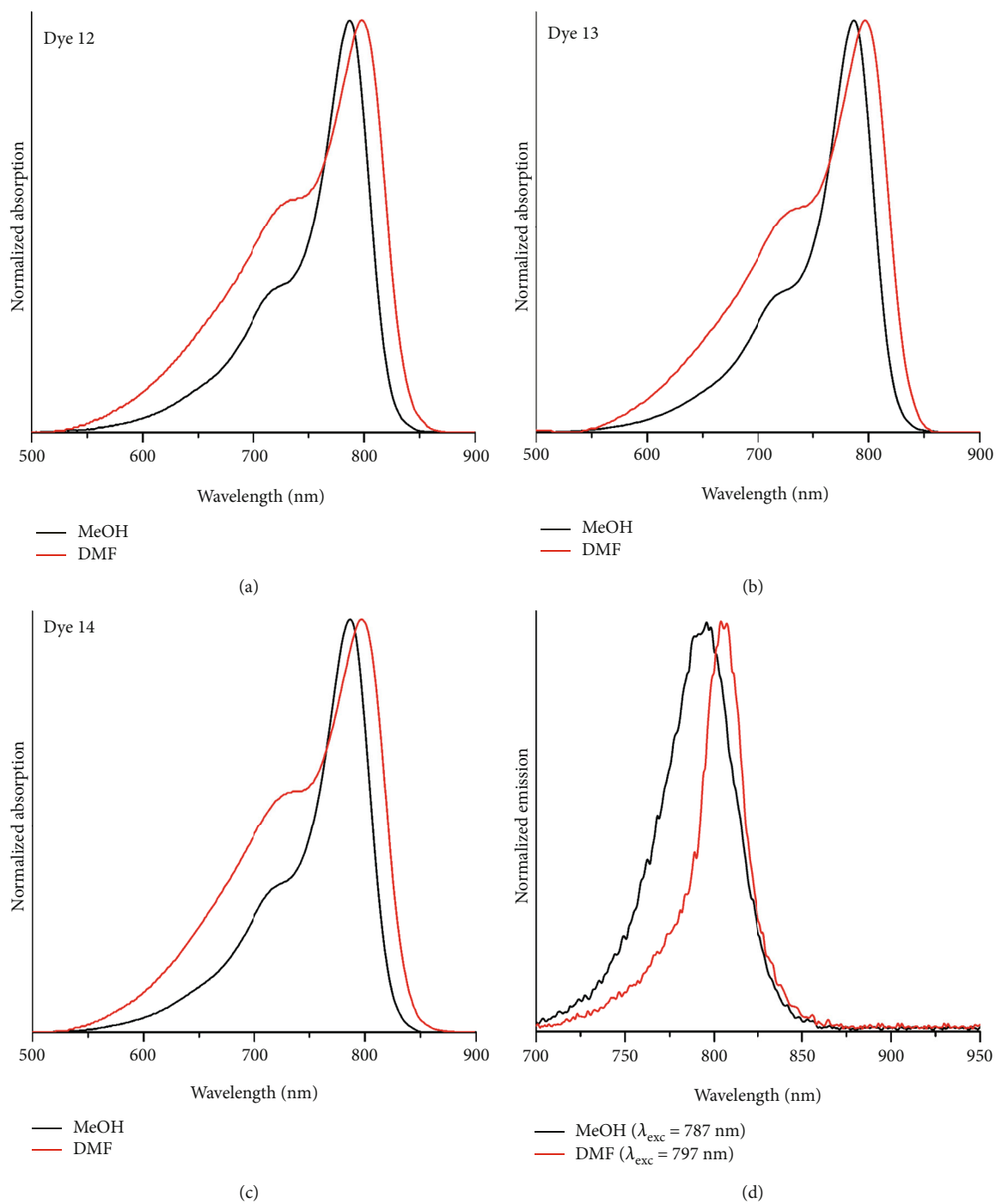


FIGURE 1: Continued.

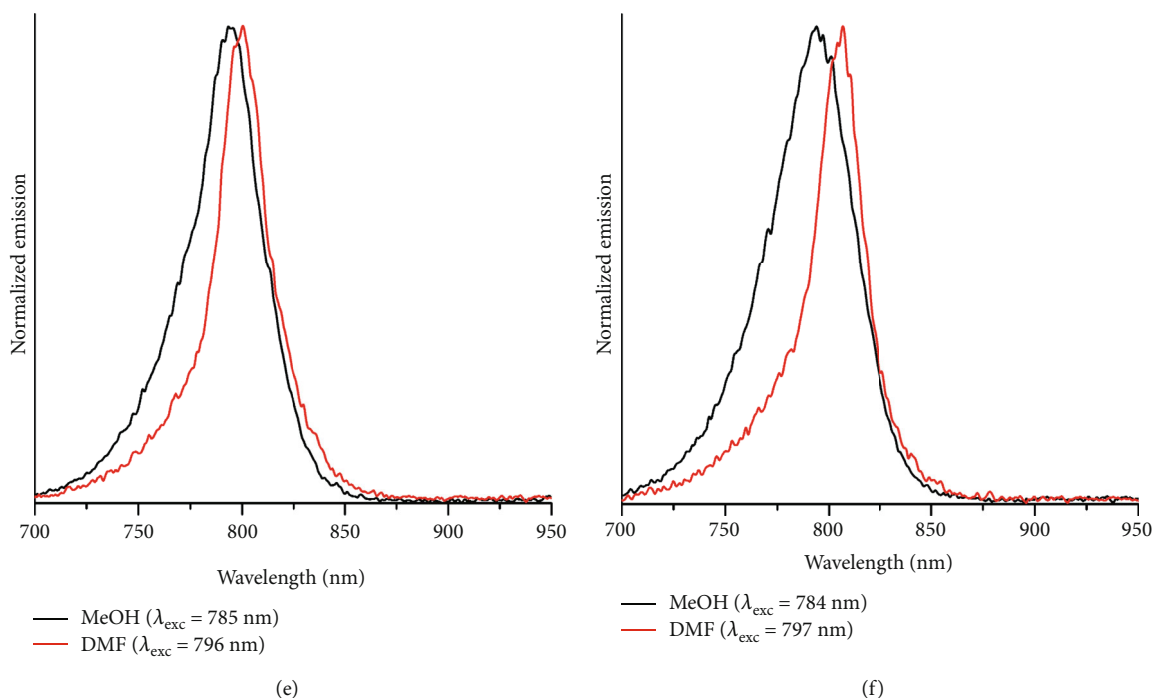
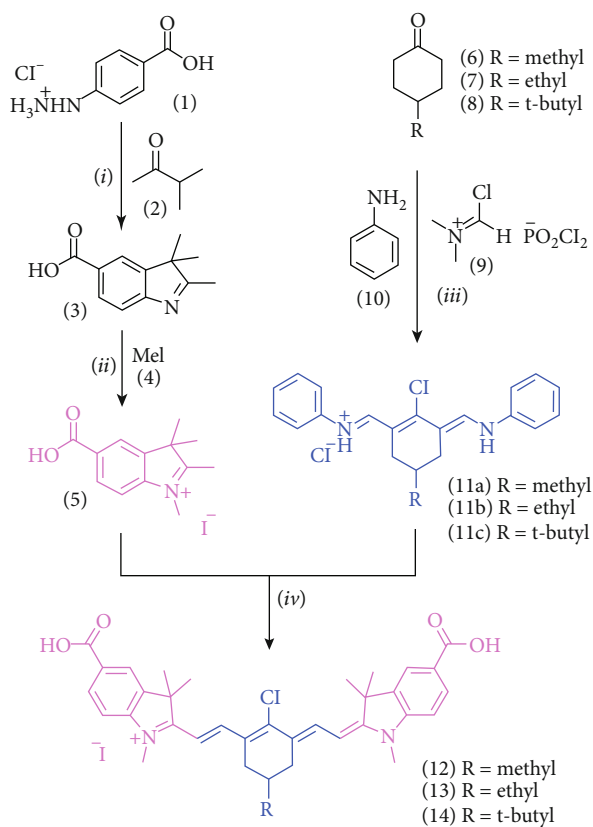


FIGURE 1: Normalized solid-state absorption spectra (DRUV) of cyanine 13 in TiO_2 film obtained from different adsorption methodologies (a) #1, (b) #2, (c) #3, (d) #4, and (e) #5. The image of the TiO_2 film sensitized under the proposed conditions of methodology #4, with 20 mM DCA (left) and 40 mM DCA (right) is also presented for comparison.



SCHEME 1: Synthesis of heptamethine cyanines 12-14, where (i) $\text{CH}_3\text{COOH}/\text{reflux}$; (ii) $\text{CH}_3\text{CN}/56^\circ\text{C}$, (iii) 1: DMF, $0-110^\circ\text{C}$, 2: aniline/EtOH, 0°C ; (iv) dark, N_2 , *i*-PrOH, $\text{CH}_3\text{COONa}/\text{reflux}$.

and under N_2 atmosphere. The final compounds were purified by precipitation and obtained in moderate yields ($\sim 50\%$). The spectroscopic characterization was performed for all intermediates and final compounds and is presented as supplementary material.

3.2. Photophysical Characterization. The UV-Vis absorption spectra of the heptamethine dyes 12-14 in the solution are shown in Figure 2. The relevant data from the photophysical characterization are summarized in Table 2. The compounds 12-14 present absorption maxima located in the NIR region, between 784 and 797 nm. The molar absorptivity coefficient values ($\epsilon \sim 105 \text{ cm}^{-1} \cdot \text{M}^{-1}$) indicate allowed electronic transitions, which could be related to $^1\pi\pi^*$ transitions. For conjugated systems, these transitions are associated with a small optical band gap ($E_g^{\text{opt}} \sim 1.4 \text{ eV}$) between the HOMO and LUMO orbitals compared to chromophores that absorb in the Vis-NIR region.

The shape of the absorption bands in Figure 2 indicates an influence of vibrational and intermolecular interactions. The decrease of vibrational interactions leads to a narrowing of the absorption band, while the increase of intermolecular interactions leads to an enlargement of the absorption band. A less intense absorption band was observed around 720 nm. Although, according to the literature, this peak could be related to the formation of H-type aggregates [16, 20, 22, 37], its intensity suggests that, in this case, this band seems to be related to $\text{S}_0 \rightarrow \text{S}_2$ electronic transitions. In fact, the formation of these aggregates in solution could be related to the lower solubility of these compounds in more polar solvents, leading to the formation of self-organized structures allowed

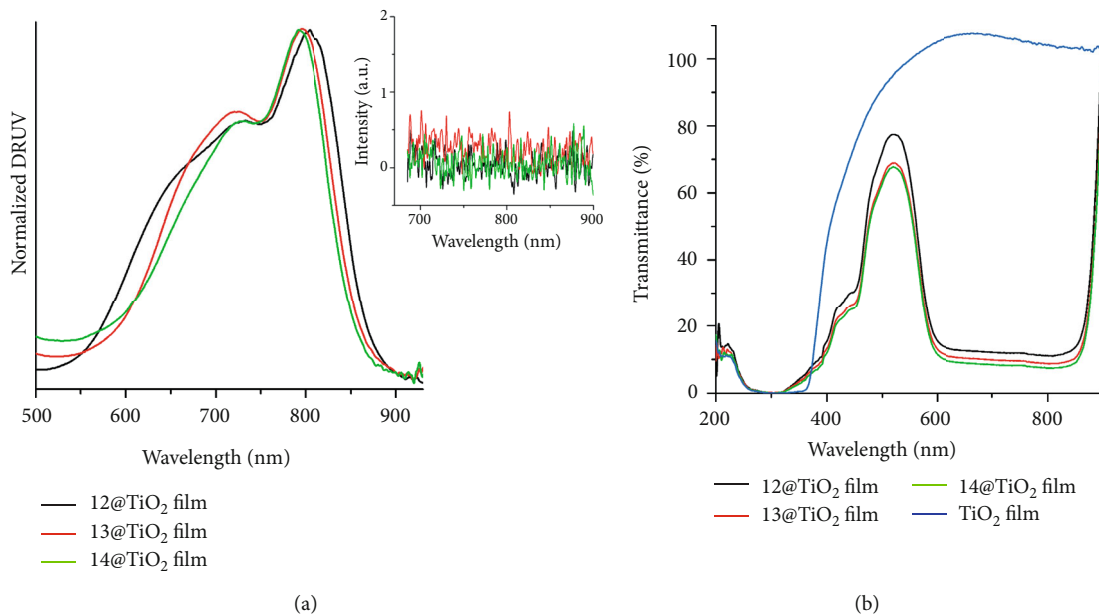


FIGURE 2: Normalized (a–c) Vis-NIR and (d–f) fluorescence emission spectra in solution (10^{-6} M) of the carboxy heptamethine dyes 12-14.

TABLE 2: Photophysical data of compounds 12-14 in solution, where λ_{abs} and λ_{em} are the absorption and emission wavelengths, respectively; ϵ ($\times 10^5$) is the molar absorptivity coefficient, $\Delta\lambda_{\text{ST}}$ is the Stokes shift; and E_g^{opt} is the optical bandgap.

Dye	Solvent	λ_{abs} (nm)	ϵ ($M^{-1}\cdot\text{cm}^{-1}$)	λ_{em} (nm)	$\Delta\lambda_{\text{ST}}$ (nm/ cm^{-1})	E_g^{opt} (eV)
12	DMF	797	1.13	805	8/125	1.45
	CH ₃ OH	787	2.46	793	6/96	1.48
13	DMF	796	1.09	800	4/63	1.45
	CH ₃ OH	785	3.16	794	9/144	1.48
14	DMF	797	1.39	805	8/125	1.48
	CH ₃ OH	784	3.22	793	9/145	1.45

by van der Waals interactions, hydrogen bonds, or hydrophobic interactions [16, 19].

In order to better characterize their photophysics, emission spectra were obtained from both absorption bands (~ 720 nm and ~ 800 nm) indicating similar location with different intensities, as expected by Kasha's rule (Figures S28-S30). In addition, the respective excitation spectra (Figures S31-S33) also presented a similar shape and location if compared to the UV-Vis spectra, which corroborates with the expected $S_0 \rightarrow S_2$ for the absorption band around 720 nm.

The fluorescence emission spectra of compounds 12-14 present emission maxima located between 793 and 805 nm. As expected, very small Stokes shifts were computed for these compounds (below 10 nm experimentally; 25 nm theoretically) due to their symmetrical nature and rigidity. These small Stokes shifts are supported by the very small change in the molecular geometries going from the ground to the first excited state and by the localized character of this $^1pp^*$ transition.

The photophysical behavior of compounds 12-14 was also evaluated in the solid state by absorption and fluorescence emission spectra (Figure 3), for the dyes adsorbed on the TiO₂ mesoporous films (guest-host system). This investigation is of great importance to evaluate the potential of these

compounds for application in dye-sensitized solar cells. The studied compounds showed outstanding adsorption on TiO₂, which can be justified by the presence of carboxyl moieties, known as good anchoring groups [38]. A very broad absorption band with maxima located in the near-infrared region is observed between 794 and 804 nm. This absorption band presents the full width at half maximum (FWHM) around 180 nm (213 nm (12), 185 nm (13), and 167 nm (14)) when compared to the results in methanol (53 nm (12), 51 nm (13), and 50 nm (14)) or DMF (112 nm (12), 105 nm (13), and 119 nm (14)) solution. Additionally, an intense blue-shifted band was found between 724 and 731 nm, different than what was observed in the solution and probably related to the formation of type H-aggregates, favored by a large number of molecules on the surface of TiO₂. It is worth mentioning that the formation of H-aggregates can be a major disadvantage when the application to solar cells is envisaged. The strong aggregation of these molecules can lead to a drastic decrease of electron injection in the TiO₂ conduction band, reducing the conversion efficiency of solar cells [20]. However, despite the presence of such aggregates, the broad absorption band in the solid-state is very important for sensitization of semiconductors and subsequent application in solar cells sensitized by

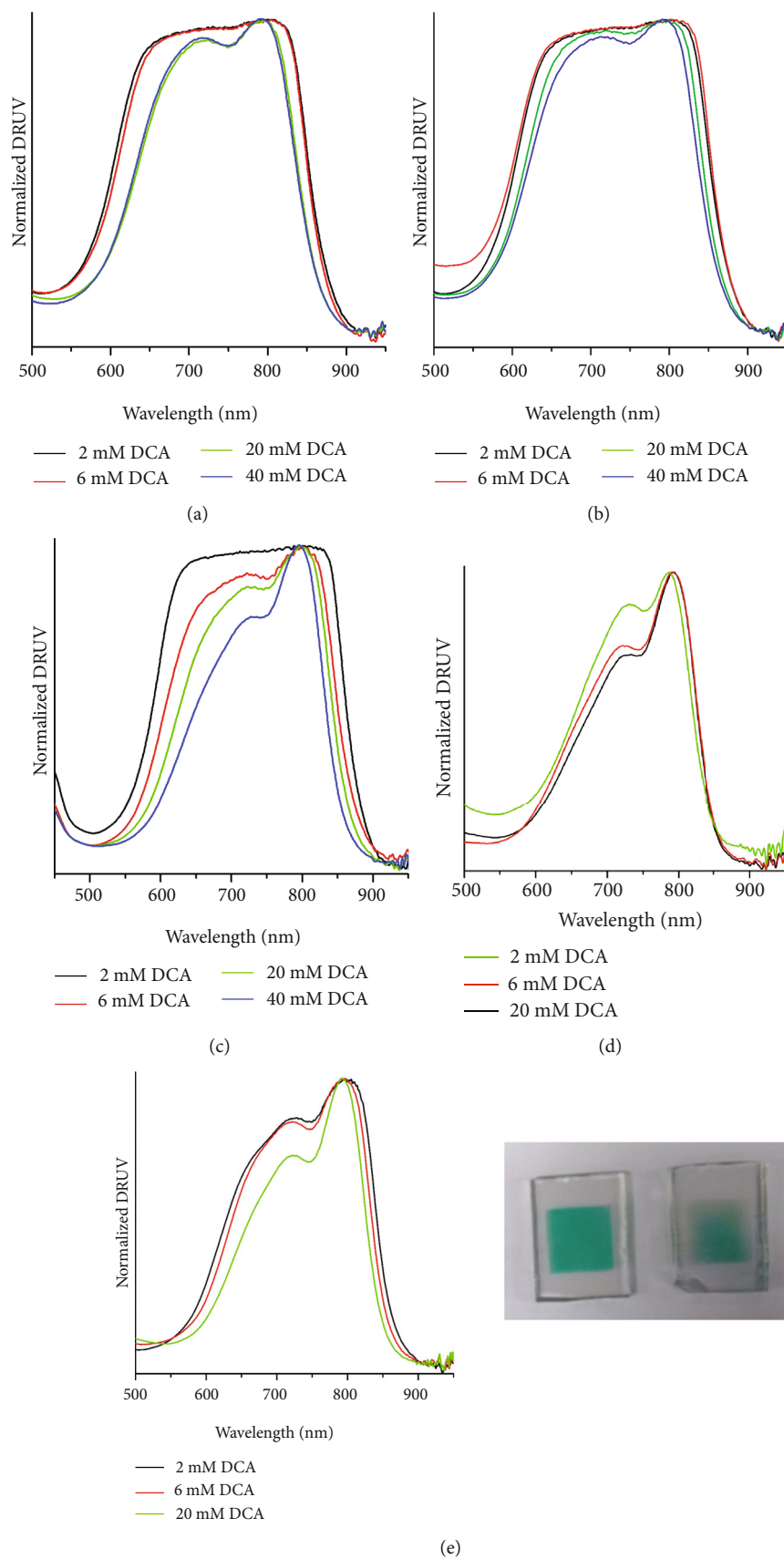


FIGURE 3: (a) Normalized UV-Vis spectra in the solid state of compounds 12-14 adsorbed on TiO_2 (powder) and (b) transmittance spectra of TiO_2 film adsorbed with compound 13. The inset presents the fluorescence emission ($\lambda_{\text{exc}} = 794 \text{ nm}$) investigation of these samples.

organic dyes, since a broader absorption range results in an optimized photon collection and, consequently, in a greater generation of electron-hole pairs and higher efficiency in converting light into electrical current. Additionally, the emission spectra of compounds 12-14 show a complete fluorescence quenching (Figure 3, insert).

The transmittance spectra of TiO₂ films sensitized by compounds 12-14 are also presented in Figure 3, where it is possible to observe the very low transmittance (~12%) in the region between 540 and 895 nm, followed by the increase of the transmittance (up to 80%) between 485 and 535 nm, which can be related once again to the significant adsorption of these compounds on TiO₂. Based on the solid-state results presented so far, it can be observed that the H-aggregates are present, which can impair the efficiency of solar cells prepared with these compounds. To minimize the formation of H-aggregates of compounds 12-14 on the surface of TiO₂, a coadsorption study was performed with deoxycholic acid (DCA). DCA is sterically bulky, and for this reason, it is expected to hinder the H-aggregation formation [20]. In this way, five different methodologies of adsorption on the mesoporous TiO₂ films were proposed and evaluated using compound 13 as a model (Table 1). In this study, the aggregation effect was evaluated taking the intensity of the H-aggregate absorption band located around 700 nm into account (Figure 1). It is worth mentioning that, based on the original data (not shown, see supplementary material Figures S34), signal saturation was discarded in Figures 1(a) and Figures 1(b) (2 and 6 mM DCA) and Figure 1(c) (2 mM DCA). This result clearly indicates that aggregation influences the shape and intensity of the solid-state UV-Vis spectra of these compounds. Additionally, based on the absorbance intensities, a higher dye loading could be obtained at 20 mM DCA for #1, #2, #4, and #5 and 6 mM DCA for #3.

DRUV spectra obtained from the first used methodology (#1) show that a small concentration of coadsorber (2 mM) results in the formation of an absorption band located at higher energy, attributed to H-aggregates, which present the same intensity of the absorption band related to the monomeric form related to the cyanine dye (Figure 1(a)). A similar result was observed using 6 mM DCA. At higher DCA concentrations (20 mM and 40 mM), a significant decrease in the intensity of the absorption band related to H-aggregates is observed, indicating more efficient aggregation suppression. Due to the strong interaction between these cyanine dyes, probably by π -stacking, the total suppression of the aggregation was not observed at the studied DCA concentrations. By comparing Figures 1(a) and 1(b), the evolution of absorption spectra along with the increase in DCA concentration is similar for methods #1 and #2, and changes in the TiO₂ temperature during adsorption is found to not play a significant role in the aggregation suppression. Based on these results, the adsorption temperature was fixed at 22°C to the next methodologies. In methodology #3, the influence of the adsorption time on the formation of aggregates is clearly observed by the significant decrease in the absorption band at 724 nm (Figure 1(c)). Based on studies described in the literature about the formation of H-

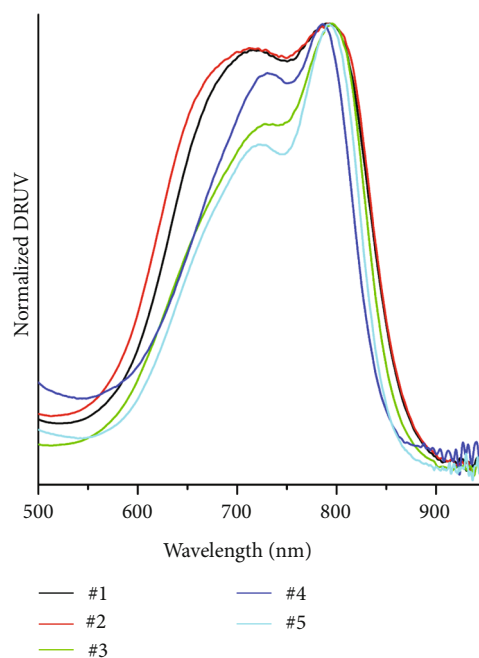


FIGURE 4: Normalized solid-state absorption spectra of dye 13 obtained from the different adsorption methodologies (#1-#5), where #1: dye concentration—5.0 mM, DCA concentrations—20 or 40 mM, TiO₂ temperature—80°C, and adsorption time—24 h; #2: dye concentration—5.0 mM, DCA concentration—40 mM, TiO₂ temperature—22°C, and adsorption time—24 h; #3: dye concentration—5.0 mM, DCA concentration—40 mM, TiO₂ temperature—22°C, and adsorption time—1 h; #4: dye concentration—0.1 mM, DCA concentration—20 mM, TiO₂ temperature—22°C, and adsorption time—1 h; #5: first step: DCA concentration—20 mM and second step: dye concentration—0.1 mM, TiO₂ temperature—22°C, and adsorption time—1 h.

aggregates in heptamethine cyanines [16, 20, 22], the concentration of 13 was fixed at 0.1 mM. Due to the low dye loading on TiO₂ when using the reduced concentration of cyanine (0.1 mM) and 40 mM of DCA, for methodologies #4 and #5, only solutions containing 2, 6, and 20 mM DCA were studied. Figure 1(d) shows this unlike what was earlier observed for #1, #2, and #3 when using methodology #4. DCA concentration plays a very important role in the formation of H-aggregates, where the lowest aggregate formation was observed using 20 mM DCA. To reduce the competition between the cyanine dye and DCA molecules for active sites in the TiO₂ surface, a fifth methodology was proposed. As one can observe, the DRUV spectra from #5 using 2 and 6 mM of DCA are similar. However, at higher concentrations of DCA (20 mM), the decrease in absorption band related to the H-aggregates is very significant. These results show that a good compromise between the lowest proportion of the H-aggregate and the best homogeneity of sensitization was obtained using one hour of adsorption, 0.1 mM dye concentration, and 20 mM DCA concentration (Figure 4).

3.3. Theoretical Calculations

3.3.1. Natural Transition Orbitals and Structural Parameters.

From the theoretical calculations, it was possible to confirm

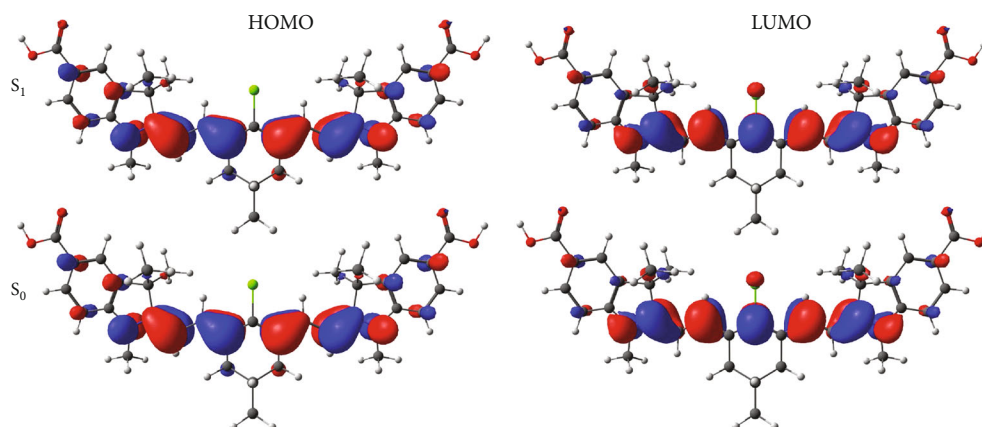


FIGURE 5: Natural transition orbitals for the vertical transitions $S_0 \rightarrow S_1$ and $S_1 \rightarrow S_0$ involving the ground and first excited states of cyanine 12 in PCM/methanol.

that the lowest-energy electronic transition $S_0 \rightarrow S_1$ is dominated by HOMO to LUMO and has a ${}^1\pi\pi^*$ character, as depicted in Figure 5 for cyanine 12. The natural transition orbitals, NTOs, associated to this transition show that the pair hole/particle, which, in this case, is identical to HOMO (hole) and LUMO (particle), is mainly delocalized in the central part of the molecule, comprised between the two heterocyclic rings. Similar behavior was observed for the other studied cyanines (Figures S24-S25). A large oscillator strength (Table S1) and strong overlap between the frontier orbitals involved in this transition were also observed, suggesting an electronic excitation of localized character. Table S1 also shows absorption and emission maxima wavelength obtained with TD-DFT. No significant differences on these values were observed by changing the alkyl group attached to the central ring, in accordance with the experimental results. This result is expected since the change in the R groups does not have a significant impact in the molecular geometry and the R group is not directly involved in the lowest-energy electronic transition. Yet, no significant change in the vertical electronic transitions was observed by changing the solvent from methanol to DMF, which was expected since both solvents have similar dielectric constants and the PCM model is not able to describe the effect of hydrogen interactions. In fact, the experimental results confirmed that the protic solvent has a very small effect on the UV-Vis spectra in the liquid phase. It is worth mentioning that the vertical transitions obtained with M06-2X functional are within the average margin of error obtained for cyanine dyes computed with TD-DFT [26]. For the studied cyanines, an average error of 0.13 eV and 0.08 eV was found for the S_0 and S_1 , respectively, when compared to the experimental values.

As can be seen in Figure 6 using compound 13 as a model, S_0 and S_1 optimized geometries are planar and symmetrical. For the other cyanines studied, see Figures S26-S27. Although very small, the main differences between the S_0 and S_1 are observed in the alternated single-double bond lengths, due to the character of the electronic transition. Since this transition does not involve the carbonyl group, the C-O bond length is preserved. The very mild difference

between these two states is also reflected in the subtle change in the dipole moment (Table S1), supporting the localized character of the transition and the lack of solvent effect on the lowest electronic transitions.

The structural parameters for dyes 12-14 are listed in Table S3. Apart from $\langle C10C9C20C21 \rangle$, which involves a sp^3 carbon atom, all the remaining dihedral angles listed in the table are nearly 180 degrees, meaning that the molecules present a high degree of planarity in both S_0 and S_1 states. Yet, the molecules present a high degree of delocalization through its π system, as evidenced by the bond length pattern in the conjugated system. Thus, the donor, acceptor groups, π -bridge, and anchor groups (-COOH) are coplanar, which would enhance the delocalization of π electrons and, thus, the intramolecular electron transfer through it. As can be seen from the frontier molecular orbital plots and confirmed by the ESP maps (Figure 7), the S_0 to S_1 excitation has a local character (which is reflected in the bond length pattern change), without any evidence of charge transfer.

3.3.2. Energy Levels and Charge Separation. The calculated energy levels of HOMO, LUMO, and band gap are presented in Table S2. The energy level diagram is presented in Figure 8. It is worth noticing that the calculated HOMO and LUMO energy levels are very sensitive to the method (basis set and functional) and can be very inaccurate due to the electron self-interaction error in DFT, providing LUMO energies with nonphysical meaning. A more accurate way to obtain HOMO-LUMO energies is using the vertical ionization potential (IP) and electron affinity (EA). This procedure is known as the Δ SCF approach [39]. In this approach, the HOMO and LUMO energies are obtained using the electronic energies of the neutral (M), cation (M^+), and anion (M^-) according to the following [40]:

$$IP = E(M^+) - E(M), \quad (1)$$

$$EA = E(M) - E(M^-). \quad (2)$$

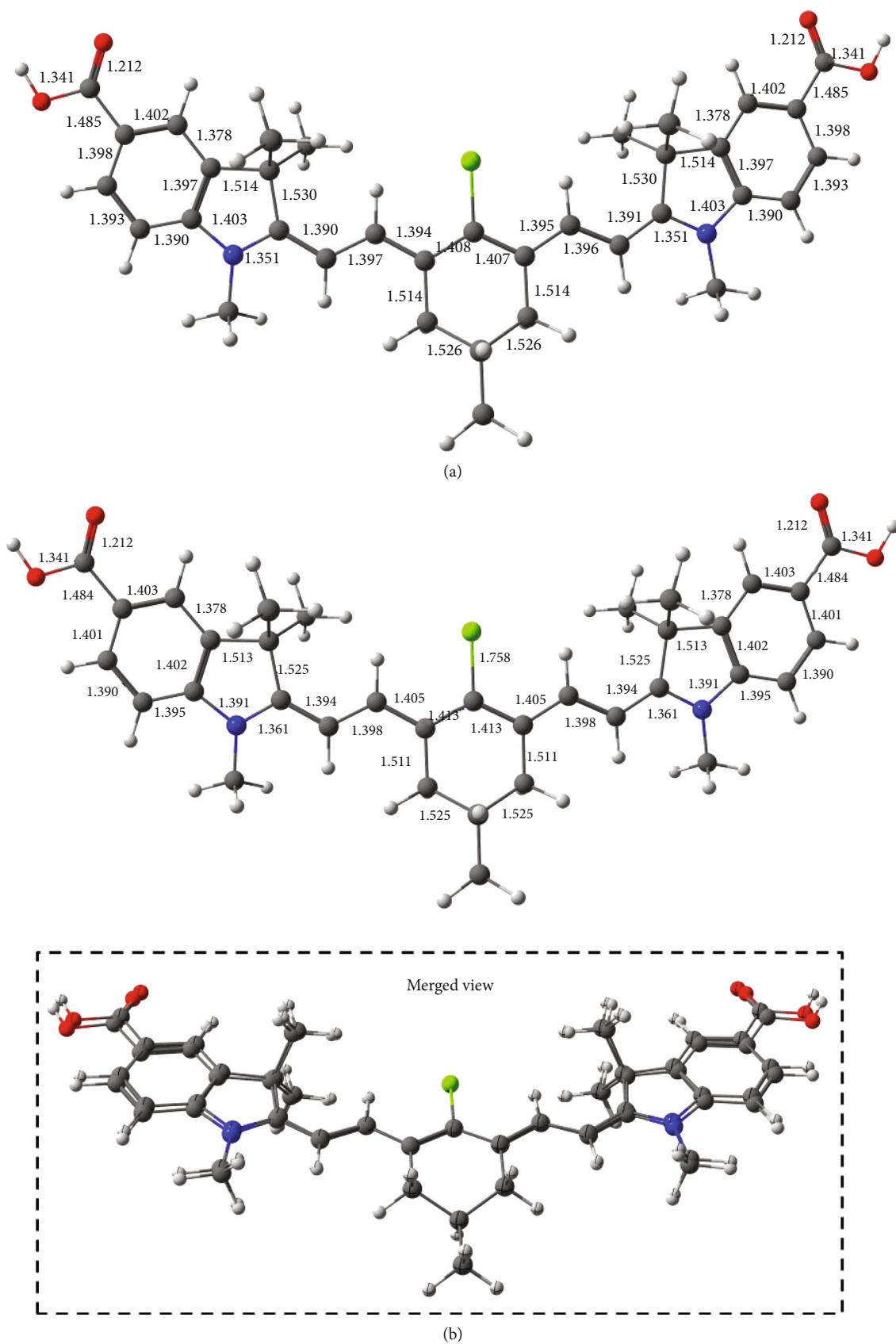


FIGURE 6: Optimized geometries for the (a) ground and (b) first excited states of cyanine 13 in PCM/methanol. A merged view (S₀ and S₁) was presented for comparison.

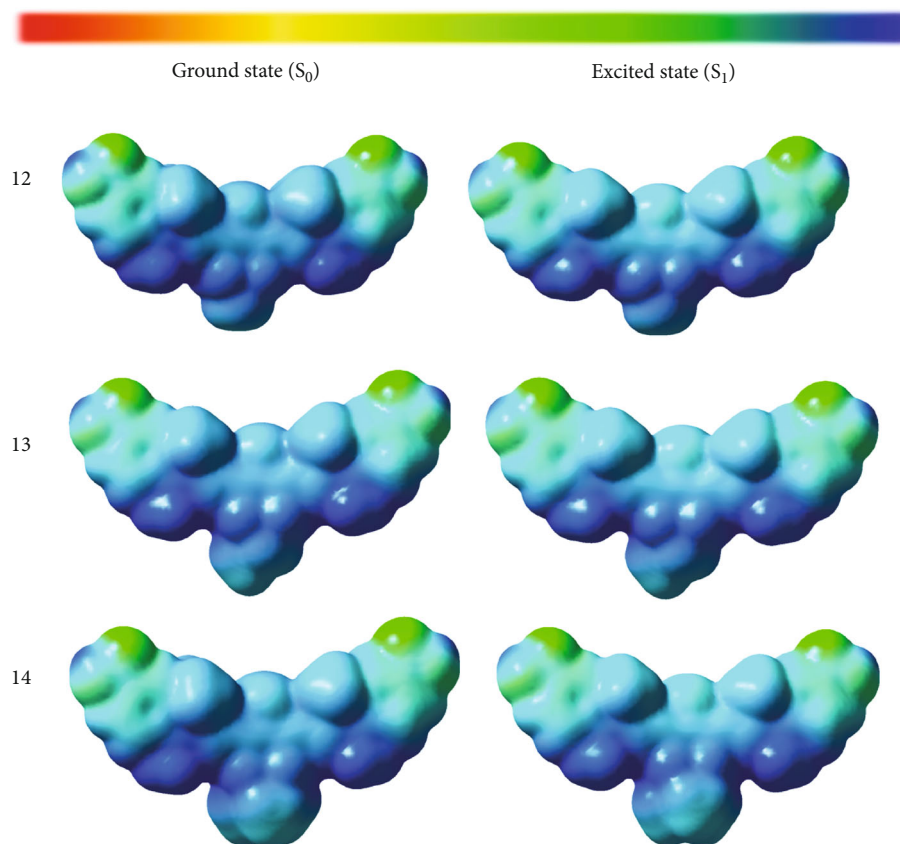


FIGURE 7: Electrostatic potential surfaces computed at M06-2X/6-311+G(d,p)//M06-2X/6-31G(d,p) in PCM/methanol for the dyes 12-14 in the ground and excited states.

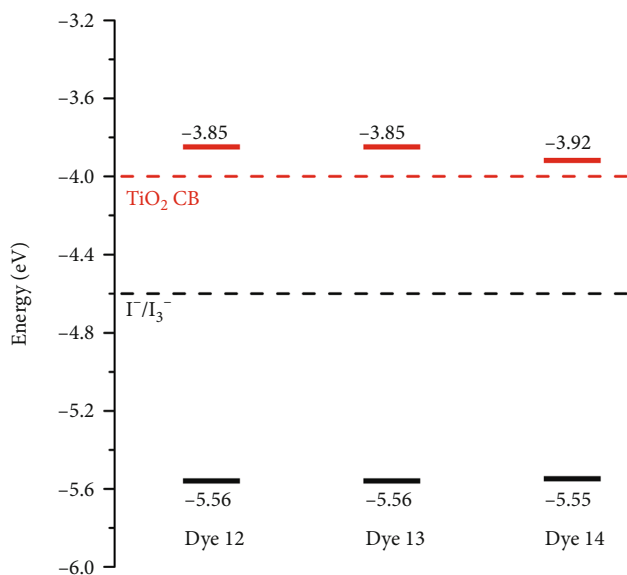


FIGURE 8: Energy level diagram. Δ SCF HOMO and LUMO energies (in eV) computed at M06-2X/6-311+G(d,p)//M06-2X/6-31G(d,p) in PCM/methanol.

Thus, the IP and EA are directly related to HOMO and LUMO energies by Koopmanns' theorem through the relations $\text{IP} = -E_{\text{HOMO}}$ and $\text{EA} = -E_{\text{LUMO}}$. Due to the

TABLE 3: Electrochemical properties of compounds 12-14, where $E_{\text{oxi}}^{\text{onset}}$ is the onset potential of oxidation, $E_{\text{red}}^{\text{onset}}$ is the onset potential of reduction, IP (HOMO) is the ionization potential, EA (LUMO) is the electron affinity, and $E_{\text{gap}}^{\text{ele}}$ is the electrochemical bandgap.

	12	13	14
$E_{\text{oxi}}^{\text{onset}}$ (V)	0.360	0.350	0.480
$E_{\text{red}}^{\text{onset}}$ (V)	-0.51	-0.55	-0.54
IP (HOMO) (eV) ^a	-4.80	-4.79	-4.92
EA (LUMO) (eV) ^b	-3.93	-3.89	-3.90
$E_{\text{gap}}^{\text{ele}}$ (eV)	0.87	0.90	1.02

^aCalculated using Equation (1); ^bcalculated using Equation (2).

approximations in the exchange-correlation functionals, this theorem can be no longer valid at the DFT level, i.e., the IP and EA are not truly equivalent to the HOMO and LUMO Kohn-Sham orbital energies, respectively. Therefore, in this work, the band gap is calculated taking the difference between EA and IP. Using this procedure, we have obtained a very good agreement with the optical gap (Δ_{opt}), i.e., the lowest vertical excitation calculated by TD-DFT. On the other hand, the energy gap is overestimated when determined directly from HOMO and LUMO energies provided by DFT calculations (Kohn-Sham gap). This discrepancy suggests that a simple estimate of the

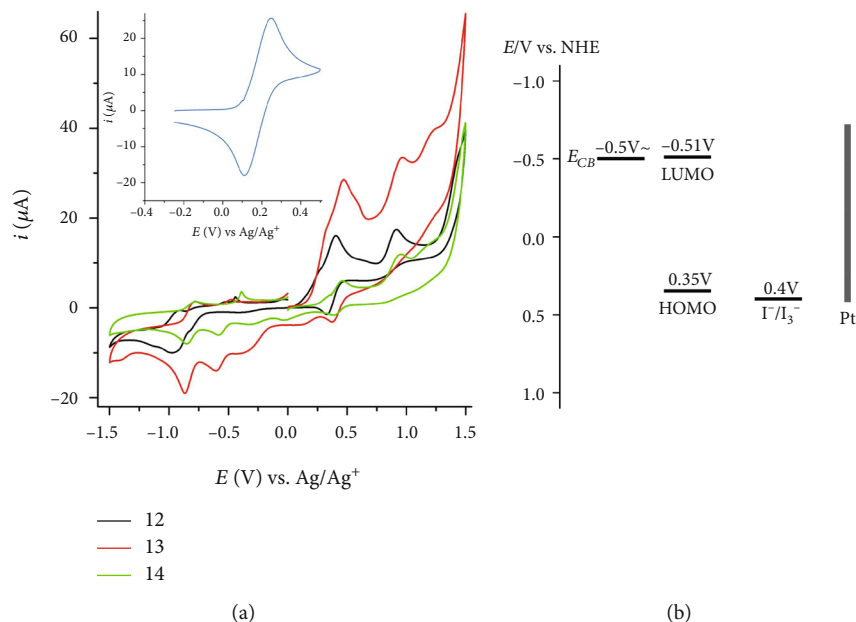


FIGURE 9: (a) Cyclic voltammogram of a glassy carbon electrode in 0.1 TBAPF₆/CH₂Cl₂ at 100 mV·s⁻¹ of cyanine dyes 12-14. Inset: voltammogram of ferrocene. (b) Energy diagram of TiO₂, cyanine 13, and the electrolyte I⁻/I₃⁻.

excited state energy using the Kohn-Sham eigenvalues for HOMO and LUMO is not appropriate for dyes 12-14.

Another way to obtain the energy levels is by computing the excited state (corresponding to the LUMO energy) as a sum between the ground state energy (HOMO energy) and the optical gap (Δ_{opt}) according to the following expression [41, 42]:

$$E_{\text{dye}^*} = E_{\text{dye}} + \Delta_{\text{opt}}. \quad (3)$$

For dyes 12-14, the optical gap is equal to 1.70 eV. Thus, following the expression above, the calculated LUMO energy is -4.76 eV (see Table S2). Although the calculated energy gaps are bigger than the experimental values provided in Table 3, a very good agreement is observed for the EA energies. These LUMO energies are slightly above the experimental anatase conduction band (CB) minimum (-4.00 eV) [43]. This would lead to the electron injection from excited dye molecules into the TiO₂ CB. The calculated and experimental values obtained for the IP (HOMO energies) are more negative than the I⁻/I₃⁻ redox potential (-4.6 eV) [44]. Thus, theoretically the relative position of HOMO and LUMO energy level in the dyes 12-14 would ensure an injection of the electrons in the TiO₂ CB and efficient dye regeneration. The similar energy gaps and HOMO-LUMO energies indicates a similar electron-injection and regeneration for the three dyes considered in this work.

3.3.3. Light Harvesting Efficiency (LHE). Light harvesting efficiency (LHE) is another important factor that determines the efficiency of a DSSC. It can be determined by [45]

$$\text{LHE} = 1 - 10^{-A} = 1 - 10^{-f}, \quad (4)$$

where f is the oscillator strength corresponding to the absorption energy of the dye. From this relation, is clear that higher oscillator strength implies larger LHE values and higher photocurrent. The LHE values obtained from TD-DFT calculation are presented in Table S2. As a consequence of the larger oscillator strengths, LHE values are very close to the unity, indicating an efficient photocurrent.

3.4. Electrochemical Characterization. To determine experimentally the relative position of the energy levels of the studied cyanine dyes 12-14, cyclic voltammeters were performed in the solution (Figure 9). The relevant data from this investigation are summarized in Table 3. The HOMO and LUMO energy levels of 12-14 were determined by the ionization potential (IP) and electron affinity (EA), respectively, which could be correlated with electrochemical processes accessed by CV, where the potentials were standardized with a Fc/Fc⁺ couple. The IP and EA values were calculated using the following empirical equations [46]:

$$\begin{aligned} \text{IP} &= -(E_{\text{oxi}}^{\text{onset}} + 4.44) \text{ eV}, \\ \text{EA} &= -(E_{\text{red}}^{\text{onset}} + 4.44) \text{ eV}, \end{aligned} \quad (5)$$

where $E_{\text{oxi}}^{\text{onset}}$ and $E_{\text{red}}^{\text{onset}}$ are the oxidation and reduction onset potentials, respectively.

Through the comparative analysis of the voltammograms (Figure 7(a)) and the data presented in Table 3, it is possible to observe that these results are not satisfactory since, considering the small difference between the averaged values of their reduction potential (~ -0.53 V) and the edge value of the TiO₂ conduction band (0.5 V), recombination processes can be favored. Based on the oxidation potential values obtained for compounds 12-14, it can be observed that they are not favorable for an efficient process of dye regeneration

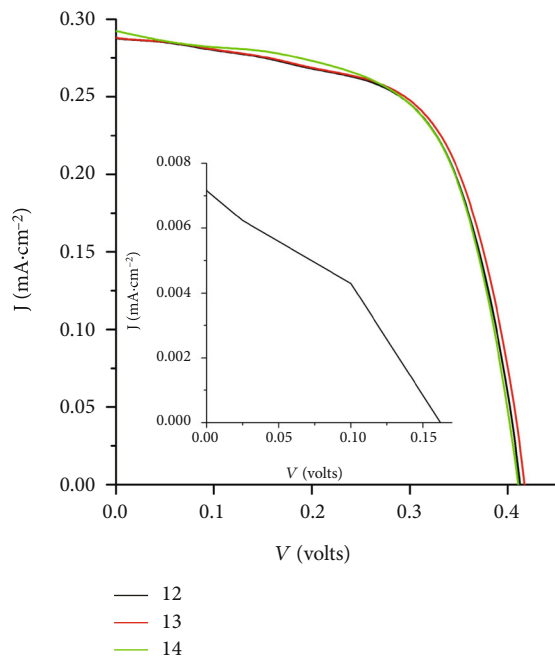


FIGURE 10: J vs. V curves from DSSCs sensitized with cyanines 12-14. The inset shows the J vs V curve from the device assembled with 13 without the coadsorption of DCA.

by the electrolyte when composed of an I^3^-/I^- (0.4 V) redox pair (Figure 9(b)).

3.5. Photoelectrochemical Characterization. Photophysical studies presented in Figure 5 have shown that method #5 was the most efficient approach allowing high dye loading and low H-aggregation; hence, DSSCs were assembled using this method to absorb compounds 12, 13, and 14 and to coadsorb DCA (Figure 10). For comparison, a DSSC using compound 13 was assembled without DCA (Figure 10, inset). One can observe that the compounds 12, 13, and 14 result in DSSCs with similar electrical behaviour and efficiency (Table 4), which is expected once the compounds present very similar structures (Scheme 1). The results also show that the methyl, ethyl, and tert-butyl groups present on the cycloalkene do not affect significantly either dye loading or dye aggregation. Indeed, the presence of DCA as a coadsorber has efficiently affected the electrical parameters and the efficiency of the DSSCs. The short circuit current density (J_{sc}) ($0.28 \text{ mA}\cdot\text{cm}^{-2}$) and conversion efficiency (η) (0.07%) values, although low, show a significant improvement if compared to those obtained for the devices assembled without the coadsorber ($0.0072 \text{ mA}\cdot\text{cm}^{-2}$). The gain in DSSC performance is related to the decreased formation of H-aggregates, by the simultaneous use of deoxycholic acid as a coadditive, as observed in Figure 5 [16, 20, 22].

The low values of J_{sc} and η can be attributed to two main factors: (i) low dye concentration on the TiO_2 surface and (ii) the similar oxidation potential values of compounds 12-14 obtained for the edge of the TiO_2 conduction band, this latter being a facilitator for recombination processes. As one can observe, the introduction of DCA dramatically decreases

TABLE 4: Electrical parameters and efficiency of solar cells sensitized with compounds 12-14, where J_{sc} is the short circuit current density ($\text{mA}\cdot\text{cm}^{-2}$), V_{oc} is the open circuit voltage (V), FF is the fill factor (%), and η is the conversion efficiency (%). The measurements were carried out under one sun ($100 \text{ mW}\cdot\text{cm}^{-2}$) using AM1.5 filter.

Device	Compound	J_{sc}	V_{oc}	FF	η
1	12	0.28	0.41	64	0.07
2	13	0.28	0.41	64	0.07
3	14	0.29	0.41	62	0.07
4 ^a	13	7.2×10^{-3}	0.17	32	0.02×10^{-3}

^aWithout DCA.

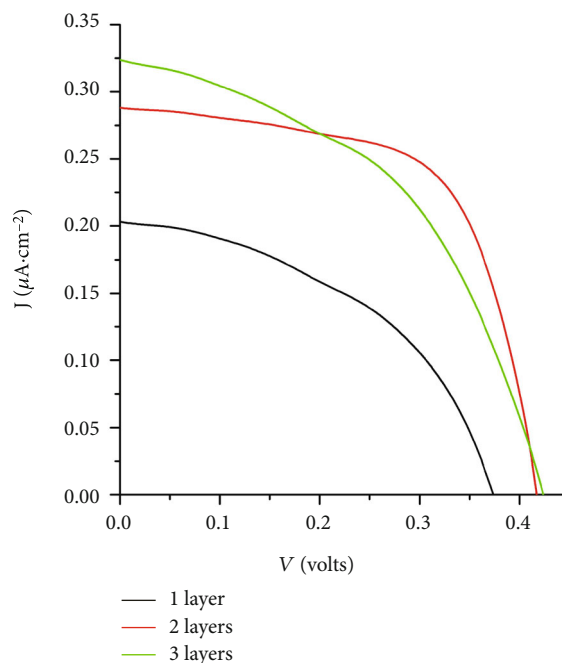


FIGURE 11: Plot J vs V of devices at different TiO_2 film thicknesses (black) $5 \mu\text{m}$ (1 layer), (red) $12 \mu\text{m}$ (2 layers), and (green) $16 \mu\text{m}$ (3 layers) prepared by methodology #5.

resistance in series and increases resistance in parallel, which is an important finding for the present system once both R_s and R_p contribute to fill factor degradation [47].

The influence of the TiO_2 film thickness on the efficiency of the devices was also evaluated. To carry out this study, devices with TiO_2 films with different thicknesses (5, 12, and 16 micrometers) were assembled. The scanning electron microscopy images show that the average thickness of the films already sintered was about $5 \mu\text{m}$ for 1 layer, $12 \mu\text{m}$ for 2 layers, and $16 \mu\text{m}$ for 3 applied layers of colloidal solution of TiO_2 nanoparticles (Figures S35). Figure 11 shows the current vs. potential curves for devices assembled with 1 up to 3 layers of TiO_2 nanoparticle colloid solution with 5-6 micrometers each and by applying the methodology #5 for sensitization.

The performance of devices assembled with 1 and 3 layers shows that the FF and V_{oc} values are affected by the thickness of the films (Table 5), while the J_{sc} values seem

TABLE 5: Electrical and efficiency parameters of solar cells with different thicknesses of the TiO₂ films, where I_{sc} is the short circuit current density (mA·cm⁻²), V_{oc} is the open circuit voltage (V), FF is the fill factor (%), and η is the conversion efficiency (%). The measurements were carried out under one sun (100 mW·cm⁻²) on masked cells (active area 0.19 cm²).

TiO ₂ thickness (μ m)	I _{sc}	V _{oc}	FF	η
5	0.21	0.35	32	0.02
12	0.28	0.41	64	0.07
16	0.29	0.34	31	0.01

not to be affected by the TiO₂ thickness. Moreover, the device with a 5 μ m layer seems to indicate a higher resistance in parallel, generated by an existing recombination mechanism. In addition, the shape of the curves and the decrease in the FF and V_{oc} values obtained for devices with 1 and 3 layers indicate that their thickness makes devices subject to higher resistance in series.

4. Conclusions

In this study, cationic carboxy heptamethine cyanines were synthesized with good yields. The photophysical characterization in methanol and DMF was performed in both ground and excited states using UV-Vis absorption and fluorescence emission spectroscopies and TD-DFT/PCM calculations. The obtained compounds showed absorption and emission in the Vis-NIR regions in the solution. The photophysical characterization in the solid state indicated that these compounds presented excellent adsorption on TiO₂, which can be justified by the presence of the carboxylic groups. The decrease of H-aggregate formation was observed by the addition of deoxycholic acid as a coadsorbent. The systematic study carried out to suppress aggregation of these dyes in the solid state allowed us to obtain an optimized methodology for sensitizing TiO₂ with the lowest number of H-aggregates. Cyclic voltammetry indicates that the LUMO values of the obtained cyanines are close to the edge of the TiO₂ conduction band. However, the HOMO and LUMO of the cyanines respect the relative positions of the energy levels for allowing charge electrotransfer to occur. Finally, the application of the studied compounds as sensitizers for TiO₂ in DSSCs showed their ability to contribute to the conversion of light into electrical energy. Additionally, when DSSCs were made by applying deoxycholic acid with compound 13 simultaneously, in the sensitization of TiO₂ films, there was a considerable increase in the conversion efficiency, short circuit current density, open circuit voltage, and fill factor values.

Data Availability

The original data supporting this study are available in the supplementary files and also from the corresponding author upon request.

Conflicts of Interest

The authors declare that they have no conflicts of interest.

Acknowledgments

We are grateful to the Coordenação de Aperfeiçoamento de Pessoal de Nível Superior (CAPES)—Finance Code 001, CNPq (409855/2018-9 and 305954/2019-9), and FAPERGS (17/2551-0000968-1) for the financial support.

Supplementary Materials

spectroscopic characterization. Additional data for DSSC preparation. Theoretical calculations. Additional photophysical data. SEM images. (*Supplementary Materials*)

References

- [1] J. L. Bricks, A. D. Kachkovskii, Y. L. Slominskii, A. O. Gerasov, and S. V. Popov, "Molecular design of near infrared polymethine dyes: a review," *Dyes and Pigments*, vol. 121, pp. 238–255, 2015.
- [2] J. Yum, P. Walter, S. Huber et al., "Efficient far red sensitization of nanocrystalline TiO₂ films by an unsymmetrical squaraine dye," *Journal of the American Chemical Society*, vol. 129, no. 34, pp. 10320–10321, 2007.
- [3] L. Beverina, J. Fu, A. Leclercq et al., "Two-photon absorption at telecommunications wavelengths in a dipolar chromophore with a pyrrole auxiliary donor and thiazole auxiliary acceptor," *Journal of the American Chemical Society*, vol. 127, no. 20, pp. 7282–7283, 2005.
- [4] P. A. Bouit, G. Wetzel, G. Berginc et al., "Near IR nonlinear absorbing chromophores with optical limiting properties at telecommunication wavelengths," *Chemistry of Materials*, vol. 19, no. 22, pp. 5325–5335, 2007.
- [5] K. B. Male and J. H. T. Luong, "An improved enzymatic assay for glucose determination in blood serum using a 1,1'-dimethylferrocenium dye," *Applied Biochemistry and Biotechnology*, vol. 61, no. 3, pp. 267–276, 1996.
- [6] C. Q. Zhu, H. Zheng, D. H. Li, S. H. Li, and J. G. Xu, "Near-infrared hydrophobic probes as molecular light switch for cmc determination of triton X-100 solution," *Chinese Journal of Chemistry*, vol. 22, no. 11, pp. 1319–1324, 2004.
- [7] L. Tarazi, N. Narayanan, and G. Patonay, "Investigation of the spectral properties of a squarylium near-infrared dye and its complexation with Fe(III) and Co(II) ions," *Microchemical Journal*, vol. 64, no. 3, pp. 247–256, 2000.
- [8] M. I. Daneshvar, J. M. Peralta, G. A. Casay et al., "Detection of biomolecules in the near-infrared spectral region via a fiber-optic immunosensor," *Journal of Immunological Methods*, vol. 226, no. 1-2, pp. 119–128, 1999.
- [9] J. Sowell, J. C. Mason, L. Strekowski, and G. Patonay, "Binding constant determination of drugs toward subdomain IIIA of human serum albumin by near-infrared dye-displacement capillary electrophoresis," *Electrophoresis*, vol. 22, no. 12, pp. 2512–2517, 2001.
- [10] X. Yang, C. Shi, R. Tong et al., "Near IR heptamethine cyanine dye-mediated cancer imaging," *Clinical Cancer Research*, vol. 16, no. 10, pp. 2833–2844, 2010.

- [11] T. Geiger, I. Schoger, D. Rentsch et al., "Unsymmetrical heptamethine dyes for NIR dye-sensitized solar cells," *International Journal of Photoenergy*, vol. 2014, Article ID 258984, 10 pages, 2014.
- [12] M. Matsui, Y. Hashimoto, K. Funabiki, J. Y. Jin, T. Yoshida, and H. Minoura, "Application of near-infrared absorbing heptamethine cyanine dyes as sensitizers for zinc oxide solar cell," *Synthetic Metals*, vol. 148, no. 2, pp. 147–153, 2005.
- [13] T. Geiger, H. Benmansour, B. Fan, R. Hany, and F. Nüesch, "Low-band gap polymeric cyanine dyes absorbing in the NIR region," *Macromolecular Rapid Communications*, vol. 29, no. 8, pp. 651–658, 2008.
- [14] W. Ghann, H. Kang, E. Emerson et al., "Photophysical properties of near-IR cyanine dyes and their application as photosensitizers in dye sensitized solar cells," *Inorganica Chimica Acta*, vol. 467, pp. 123–131, 2017.
- [15] H. Zhang, G. Wicht, C. Gretener et al., "Semitransparent organic photovoltaics using a near-infrared absorbing cyanine dye," *Solar Energy Materials & Solar Cells*, vol. 118, pp. 157–164, 2013.
- [16] T. Ono, T. Yamaguchi, and H. Arakawa, "Study on dye-sensitized solar cell using novel infrared dye," *Solar Energy Materials & Solar Cells*, vol. 93, no. 6-7, pp. 831–835, 2009.
- [17] K. Funabiki, H. Mase, A. Hibino et al., "Synthesis of a novel heptamethine-cyanine dye for use in near-infrared active dye-sensitized solar cells with porous zinc oxide prepared at low temperature," *Energy & Environmental Science*, vol. 4, no. 6, pp. 2186–2192, 2011.
- [18] G. Chen, D. Yokoyama, H. Sasabe, Z. R. Hong, Y. Yang, and J. Kido, "Optical and electrical properties of a squaraine dye in photovoltaic cells," *Applied Physics Letters*, vol. 101, no. 8, article 083904, 2012.
- [19] M. Ziółek, J. Karolczak, M. Zalas, Y. Hao, H. Tian, and A. Douhal, "Aggregation and electrolyte composition effects on the efficiency of dye-sensitized solar cells. A case of a near-infrared absorbing dye for tandem cells," *The Journal of Physical Chemistry C*, vol. 118, no. 1, pp. 194–205, 2013.
- [20] K. Pydzińska and M. Ziółek, "Solar cells sensitized with near-infrared absorbing dye: problems with sunlight conversion efficiency revealed in ultrafast laser spectroscopy studies," *Dyes and Pigments*, vol. 122, pp. 272–279, 2015.
- [21] J. H. Yum, S. J. Moon, R. Humphry-Baker et al., "Effect of coadsorbent on the photovoltaic performance of squaraine sensitized nanocrystalline solar cells," *Nanotechnology*, vol. 19, no. 42, article 424005, 2008.
- [22] C. H. Lee, H. J. Yun, M. R. Jung, J. G. Lee, S. H. Kim, and J. H. Kim, "Preparation and characterization of squaraine dyes containing mono-and bis-anchoring groups as the light absorber in dye sensitized solar cells," *Electrochimica Acta*, vol. 138, pp. 148–154, 2014.
- [23] M. J. Frisch, G. W. Trucks, H. B. Schlegel et al., *Gaussian 16, Revision A.03*, Gaussian, Inc., Wallingford CT, 2016.
- [24] Y. Zhao and D. G. Truhlar, "The M06 suite of density functionals for main group thermochemistry, thermochemical kinetics, noncovalent interactions, excited states, and transition elements: two new functionals and systematic testing of four M06-class functionals and 12 other functionals," *Theoretical Chemistry Accounts*, vol. 120, pp. 215–241, 2008.
- [25] S. Grimme, J. Antony, S. Ehrlich, and H. Krieg, "A consistent and accurate ab initio parametrization of density functional dispersion correction (DFT-D) for the 94 elements H-Pu," *Journal of Chemical Physics*, vol. 132, no. 15, pp. 154104–154119, 2010.
- [26] N. Minezawa, "Vertical excitation energies of linear cyanine dyes by spin-flip time-dependent density functional theory," *Chemical Physics Letters*, vol. 662, no. 16, pp. 115–119, 2015.
- [27] D. Jacquemin, Y. Zhao, R. Valero, C. Adamo, I. Ciofini, and D. G. Truhlar, "Verdict: time-dependent density functional theory "not guilty" of large errors for cyanines," *Journal of Chemical Theory and Computation*, vol. 8, no. 4, pp. 1255–1259, 2012.
- [28] B. Le Guennic and D. Jacquemin, "Taking up the cyanine challenge with quantum tools," *Accounts of Chemical Research*, vol. 48, no. 3, pp. 530–537, 2015.
- [29] B. Mennucci, E. Cancès, and J. Tomasi, "Evaluation of solvent effects in isotropic and anisotropic dielectrics and in ionic solutions with a unified integral equation method: theoretical bases, computational implementation, and numerical applications," *The Journal of Physical Chemistry B*, vol. 101, no. 49, pp. 10506–10517, 1997.
- [30] E. Cancès, B. Mennucci, and J. Tomasi, "A new integral equation formalism for the polarizable continuum model: theoretical background and applications to isotropic and anisotropic dielectrics," *Journal of Chemical Physics*, vol. 107, no. 8, pp. 3032–3041, 1997.
- [31] E. Cancès and B. Mennucci, "New applications of integral equations methods for solvation continuum models: ionic solutions and liquid crystals," *Journal of Mathematical Chemistry*, vol. 23, no. 3/4, pp. 309–326, 1998.
- [32] R. L. Martin, "Natural transition orbitals," *The Journal of Chemical Physics*, vol. 118, no. 11, pp. 4775–4777, 2003.
- [33] R. C. Duarte, F. S. Santos, B. Bercini et al., "Synthesis of a 5-carboxy indole-based spiropyran fluorophore: thermal, electrochemical, photophysical and bovine serum albumin interaction investigations," *Chemosensors*, vol. 8, no. 2, pp. 2–17, 2020.
- [34] C. F. H. Allen and C. V. Wilson, "The use of N15 as a tracer element in chemical reactions. The mechanism of the Fischer indole synthesis," *Journal of the American Chemical Society*, vol. 65, no. 4, pp. 611–612, 1943.
- [35] G. O. Menéndez, M. E. Pichel, C. C. Spagnuolo, and E. A. Jares-Erijman, "NIR fluorescent biotinylated cyanine dye: optical properties and combination with quantum dots as a potential sensing device," *Photochemical & Photobiological Sciences*, vol. 12, no. 2, pp. 236–240, 2013.
- [36] A. Owens, N. Bruschi, J. G. Tawney, and M. Henary, "A microwave-assisted and environmentally benign approach to the synthesis of near-infrared fluorescent pentamethine cyanine dyes," *Dyes and Pigments*, vol. 113, pp. 27–37, 2015.
- [37] H. Lee, C. Mason, and S. Achilefu, "Synthesis and spectral properties of near-infrared aminophenyl-, hydroxyphenyl-, and phenyl-substituted heptamethine cyanines," *Journal of Organic Chemistry*, vol. 73, no. 2, pp. 723–725, 2008.
- [38] P. Qui and G. J. Meyer, "Proton-controlled electron injection from molecular excited states to the empty states in nanocrystalline TiO₂," *Langmuir*, vol. 17, no. 21, pp. 6720–6728, 2001.
- [39] J. R. De Lile, S. G. Kang, Y. -A. Son, and S. G. Lee, "Do HOMO–LUMO energy levels and band gaps provide sufficient understanding of dye-sensitizer activity trends for water purification?," *ACS Omega*, vol. 5, no. 25, pp. 15052–15062, 2020.
- [40] C. G. Zhan, J. A. Nichols, and D. A. Dixon, "Ionization potential, electron affinity, electronegativity, hardness, and electron

excitation energy: molecular properties from density functional theory orbital energies,” *The Journal of Physical Chemistry A*, vol. 107, no. 20, pp. 4184–4195, 2003.

- [41] F. De Angelis, S. Fantacci, and A. Selloni, “Alignment of the dye’s molecular levels with the TiO₂ band edges in dye-sensitized solar cells: a DFT-TDDFT study,” *Nanotechnology*, vol. 19, no. 42, article 424002, 2008.
- [42] C. I. Oprea, P. Panait, Z. M. Essam, R. M. Abd El-Aal, and M. A. Gîrțu, “Photoexcitation processes in oligomethine cyanine dyes for dye-sensitized solar cells—synthesis and computational study,” *Nanomaterials*, vol. 10, no. 4, p. 662, 2020.
- [43] M. Gratzel, “Photoelectrochemical cells,” *Nature*, vol. 414, no. 6861, pp. 338–344, 2001.
- [44] X. Jin, D. Li, L. Sun, C. L. Wang, and F. Q. Bai, “Theoretical design of porphyrin sensitizers with different acceptors for application in dye-sensitized solar cells,” *RSC Advances*, vol. 8, no. 35, pp. 19804–19810, 2018.
- [45] C. Y. Qin and A. E. Clark, “DFT characterization of the optical and redox properties of natural pigments relevant to dye-sensitized solar cells,” *Chemical Physics Letters*, vol. 438, no. 1–3, pp. 26–30, 2007.
- [46] C. M. Cardona, W. Li, A. E. Kaifer, D. Stockdale, and G. C. Bazan, “Electrochemical considerations for determining absolute frontier orbital energy levels of conjugated polymers for solar cell applications,” *Advanced Materials*, vol. 23, no. 20, pp. 2367–2371, 2011.
- [47] R. Guliana, A. Jainb, and A. Kapoora, “Exact analytical analysis of dye-sensitized solar cell: improved method and comparative study,” *The Open Renewable Energy Journal*, vol. 5, no. 1, pp. 49–60, 2012.

Research Article

Preparation of Transparent Film of Layered Double Hydroxide with Anionic Pyrene Derivatives and Its Luminous Toluene Detection Ability

Takuya Fujimura , Yoshiya Akagashi, Yu-hei Aoyama, and Ryo Sasai 

Department of Materials Chemistry, Graduate School of Natural Science and Technology, Shimane University, 1060 Nishi-kawatsu-cho, Matsue 690-8504, Japan

Correspondence should be addressed to Ryo Sasai; rsasai@riko.shimane-u.ac.jp

Received 9 September 2020; Revised 20 November 2020; Accepted 24 November 2020; Published 7 December 2020

Academic Editor: Adel A. Ismail

Copyright © 2020 Takuya Fujimura et al. This is an open access article distributed under the Creative Commons Attribution License, which permits unrestricted use, distribution, and reproduction in any medium, provided the original work is properly cited.

To prepare the transparent solid film of layered double hydroxide, the filtration-film transfer (FFT) method using LDH nanosheet colloidal suspension was investigated. It was found that the homogeneous LDH solid film with enough transparency in the visible light range could be prepared by the FFT method. Moreover, anionic pyrene (Pyr^-) molecules could be incorporated into the transparent LDH solid film by immersing in anionic pyrene solution. From both absorption and emission spectra of the transparent Pyr^-/LDH solid film, Pyr^- incorporated in the LDH solid film formed aggregates and mainly showed the strong excimer emission. Additionally, the luminous response of the transparent Pyr^-/LDH solid film was investigated in ethanol-toluene mixed solution with various toluene contents. As results, the ratio of luminescence intensities from static excimer and monomer of incorporated Pyr^- molecules depended on the toluene content, and excimer emission decreased with an increase in the toluene content. This luminous response can be caused by an increase of the monomeric Pyr^- species, because Pyr^- aggregates are broken by adsorption of toluene molecules into the LDH interlayer space. The obtained transparent hybrid film may be useful as a detectable material of toluene in solvent by luminous change.

1. Introduction

Layered double hydroxide (LDH), which has crystal structure stacked brucite-like metal hydroxide layer with positive charges and anion species alternatively, is one of anion exchangeable inorganic layered materials, and its general chemical formula is $[\text{M}^{2+}_{1-x}\text{M}^{3+}_x(\text{OH})_2](\text{A}^{n-})_{x/n}$, where M^{2+} is the divalent cation, M^{3+} is the trivalent cation, A^{n-} is the n -valent interlayer anion, and x is the amount of trivalent cation, respectively [1–3]. It is well known that various anions such as anionic functional dyes can be intercalated into the LDH interlayer space by anion-exchange reaction. Then, it can be expected that the anionic functional dyes intercalated in the interlayer space show the unique photophysical and/or photochemical properties, which differ from those properties observed in bulk solutions. Thus, many researchers have reported the intercalation of the functional

dyes into the interlayer space of LDH, and then the photophysical and/or photochemical properties of functional dyes in LDH interlayer space have been also reported [4–8]. These reports suggested that the materials hybridizing functional dyes with LDH are one of promising material systems for various functional devices such as sensor, light emitting devices, display, and memory [9–14]. However, it is very difficult to quantitatively characterize the details of photophysical and/or photochemical properties of the most of reported hybrid systems, because the hybrid sample can be prepared as powder in usual case. To understand the nature of the functional dyes intercalated in the interlayer space of LDH and the detailed mechanism of the photofunctionalities, the transparent film sample of these hybrid materials will be required.

Some preparation techniques to obtain the transparent film consisting of layered materials such as casting,

Langmuir-Blodgett (LB), and layer-by-layer (LbL) methods have been already reported [15–18]. The casting method is very easy, but it is difficult to prepare the film with high uniformly and transparency. On the other hand, LB and LbL methods can provide the film with good uniformly and transparency. However, procedures of them are complicated, and several spectrometric analyses will be disturbed by low absorbance and/or emission intensity of the dye/layered material hybrid films prepared by these methods because of the small number of the layers in the film. Kawamata and Takagi et al. succeeded to prepare the uniform transparent thin film consisting of clay mineral and/or dye by transfer of the clay mineral and/or dye residue, which was obtained via filtration of those dispersion, on glass substrate [10, 19, 20]. This method (filtration-film transfer (FFT) method) is easy way, and the hybrid film, which have enough transparency, absorbance, and emission intensity to measure several spectroscopic techniques, consisting of dyes and clay minerals can be prepared. We reported that the transparent and uniform α -zirconium phosphate thin film can be also prepared by the FFT method. To prepare the transparent film of layered materials by the FFT method, the nanosheet colloidal dispersion, which can be prepared by delamination of layered compound by delamination reagent, is required [21]. Iyi et al. reported on the preparation of LDH nanosheet colloidal aqueous dispersion. Moreover, Iyi et al. succeeded to prepare the transparent LDH film by simple evaporation of LDH nanosheet aqueous dispersion and demonstrate the ion-exchange reaction of this film [22]. However, it is easily expected that it is hard to control the thickness and/or uniformly of the obtained film.

In this paper, we attempted to utilize the FFT method to obtain the transparent LDH film. Then, anionic pyrene derivative (pyrene-1-sulfonate, abbreviated as Pyr^-), which was used as photofunctional dye in this study, [23–25] was intercalated into the interlayer space of the LDH film to investigate the photophysical behavior of the anionic pyrene in LDH. Furthermore, we investigated the luminous response of the present film in ethanol-toluene mixed solution to explore the possibility of the present transparent hybrid film as a detectable material of toluene in solvent by luminous change.

2. Materials and Methods

2.1. Materials. 1-Pyrenesulfonic acid sodium salt (Merck) and layered double hydroxide (acquired from Kyowa chemical Industry, co., LTD.) were used as received. Stoichiometric formula of carbonate type LDH is $[\text{Mg}_3\text{Al}(\text{OH})_8](\text{CO}_3)_{0.5}$. Sodium chloride, acetic acid (AcOH), ethanol, sulfuric acid, propionic acid (PrOH), and toluene were purchased from Fujifilm Wako Pure Chemical Corporation and used as received without purification. The glass substrate (cover glass) was purchased from Matsunami Glass Ind., Ltd. The glass substrate was sonicated with water for 30 min and then treated in sulfuric acid overnight at room temperature. After that, glass substrate was washed with enough water. All water used within this work is Milli-Q water prepared by a Direct-Q UV system (Merck Millipore).

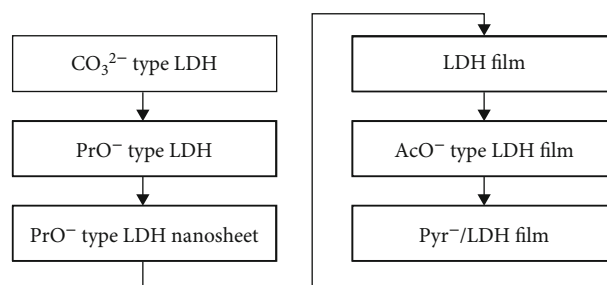


FIGURE 1: Flow chart of the experimental procedure to prepare the Pyr^-/LDH film.

2.2. Preparation of the Transparent LDH Only Film. Flow chart of the experimental procedure to prepare the Pyr^-/LDH film was shown in Figure 1. PrO^- type LDH was prepared via decarbonation and ion-exchange reaction according to literatures [22]. Obtained PrO^- type LDH (40 mg) was dispersed in 20 mL of water to obtain LDH nanosheet dispersion. 600 μL of obtained dispersion was filtered through a PTFE membrane filter (pore size = 0.1 μm), and the residue was transferred upon the glass substrate. The obtained thin film was dried up under reduced pressure condition overnight.

2.3. Preparation of the Pyr^-/LDH Film. Two pieces of the LDH only film were immersed in EtOH (300 mL) in three-neck separable flask, and solution was purged with nitrogen gas to remove the CO_2 . The concentration of CO_2 in exhausted N_2 gas was monitored with CO_2 meter (testo 535). 0.17 mL of AcOH was added in the flask, and solution was stirred overnight under N_2 flow. The film was washed with EtOH and then dried under reduced pressure condition, and the AcO^- type LDH film was obtained. The AcO^- type LDH film was immersed in Pyr^- EtOH solution (500 mL, 5.1×10^{-6} M, corresponding to 2.5% versus anion-exchange capacity of the LDH film) for 24 hours under N_2 flow. The obtained hybrid film was washed with EtOH and dried under reduced pressure condition. Amount of intercalated Pyr^- was estimated from the decreased absorbance of Pyr^- in immersion solution.

2.4. The Effect of the Toluene on Fluorescence Spectra of the Pyr^-/LDH Film. The Pyr^-/LDH film was immersed in mixture of EtOH and toluene (concentrations of the toluene are 0, 10, 30, 50, 70, 90, and 100%(v/v)) in quartz cuvette, and then the film was set at 45° against the direction of the excitation light source and the detector of emission to reduce the incident light, which is reflected excitation light by the film and substrate, to the detector. The top view of the setup for emission measurement was shown in Figure 2.

2.5. Characterization. The absorption spectra, XRD patterns, and FT-IR spectra were measured with V-750 (JASCO), Mini-Flex II (RIGAKU), and FT-IR 6100 (JASCO), respectively. The fluorescence and excitation spectra were examined through a fluorescence spectrophotometer (FP-6600, JASCO).

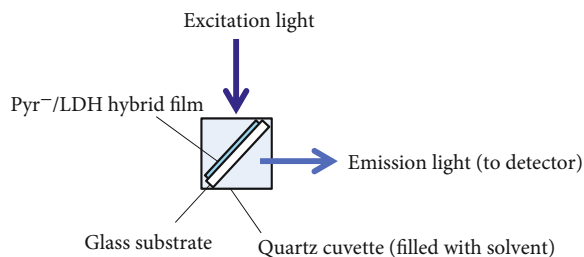
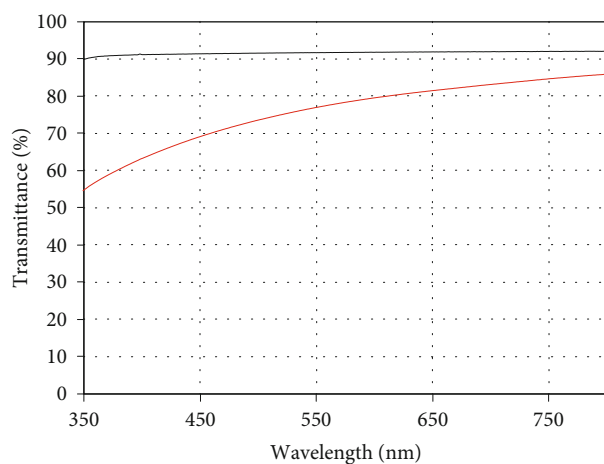


FIGURE 2: Top view of setup for emission measurement of the film (top view).



(a)



(b)

FIGURE 3: (a) Photograph of the LDH only film, (b) transmittance spectra of the LDH only film (red line), and glass substrate (black line).

3. Results and Discussion

3.1. Preparation of the LDH Only Film. In Figures 3(a) and 3(b), photograph and transmittance spectrum of the LDH film prepared by the FFT method were shown, respectively. From the photograph (see Figure 3(a)), the enough transparency of the obtained LDH solid film was visible. The transmittance of the LDH film was higher than 55% in the range of 350 to 800 nm as shown in Figure 3(b). These results indicate that the transparent LDH solid film can be prepared by the FFT method. Therefore, it is found that the FFT method is one of useful and applicable techniques for preparing the transparent solid film from LDH nanosheet suspension.

In Figure 4, the XRD patterns of the carbonate type LDH powder, PrO^- type LDH powder and LDH only film were shown.

In the XRD pattern of the LDH only film, the diffraction lines from 001 plane could be observed at 11.2° (003) and

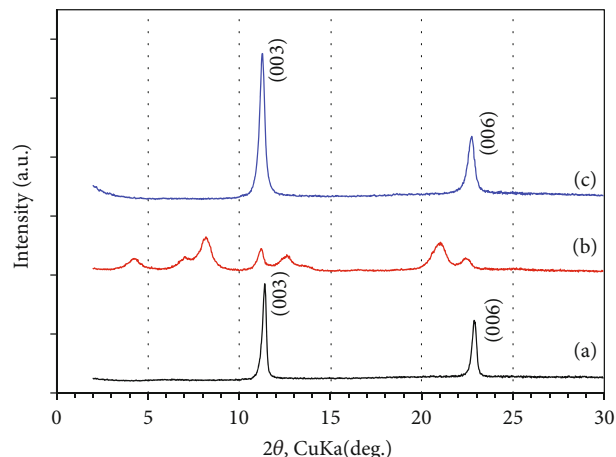


FIGURE 4: The XRD patterns of the (a) carbonate type LDH powder (black line), (b) PrO^- type LDH powder (red line), and (c) LDH only film (blue line).

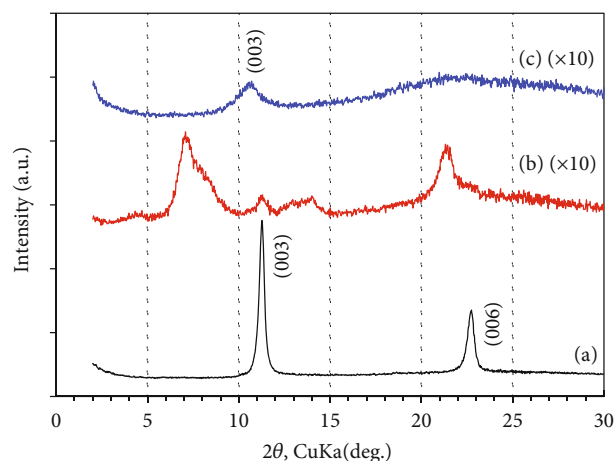


FIGURE 5: XRD patterns of the (a) LDH film (black line), (b) AcO^- type LDH film (red line), and (c) Pyr^- /LDH hybrid film (blue line).

22.7° (006), respectively. This diffraction pattern of the LDH solid film was almost the same as that of carbonate type LDH powder, but not as PrO^- type LDH powder, in which the lots of diffraction peaks were observed because of the mixed hydration and dehydration phase [22]. These results suggest that counter anion incorporated in LDH would be an exchange from PrO^- to carbonate anions during the FFT process. This consideration can be supported by the previous report by Iyi et al., which reported that carboxylate type LDH was not stable in air, and then incorporated carboxylate ion was replaced by carbonate ion. Thus, we can succeed in preparing the transparent LDH solid film with carbonate anion as exchangeable anion species by the FFT method.

3.2. Preparation of the Pyr^- /LDH Hybrid Film and Its Luminous Behavior. To hybridize Pyr^- with the LDH solid film, counter anion species in the LDH only film had to be exchanged from carbonate to AcO^- anion, because the prepared LDH solid film had carbonate anion, which is hardly exchanged into other anion species [3, 26]. The XRD patterns

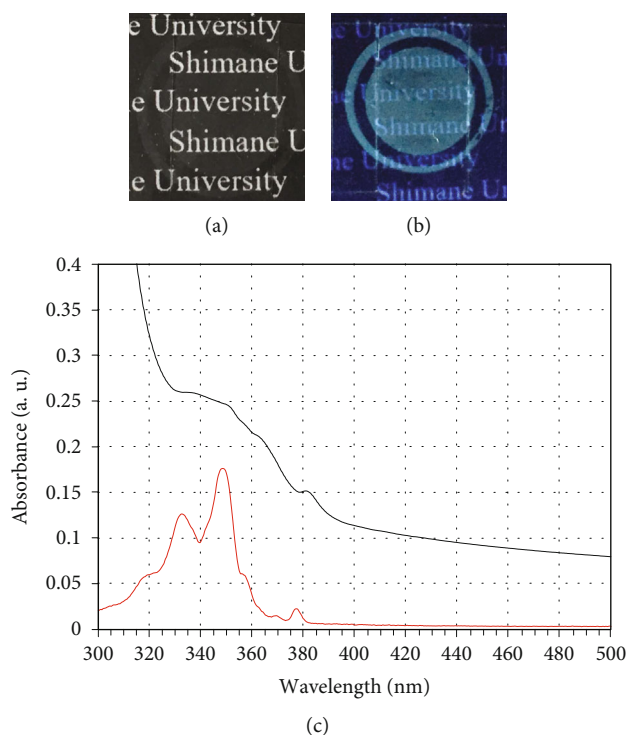


FIGURE 6: Photograph of the Pyr⁻/LDH film under (a) room light, (b) UV light irradiation (365 nm), and (c) UV-Vis absorption spectra of the Pyr⁻/LDH film (black line) and Pyr⁻ aqueous solution (1.0×10^{-5} mol/L, red line).

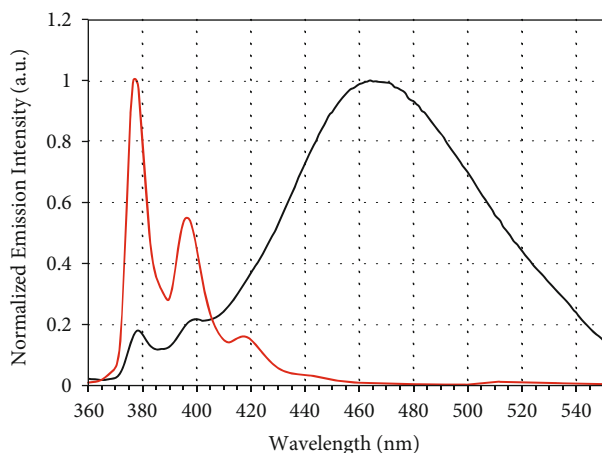


FIGURE 7: Normalized emission spectra of the Pyr⁻/LDH hybrid film in air (black line, excited at 340 nm) and Pyr⁻ aqueous solution (1.0×10^{-6} mol/L, red line, excited at 347 nm).

of the LDH solid film obtained after decarbonation treatment using ethanol-acetic acid mixed solution (see Figure 5(b)) agreed with that of AcO⁻ type LDH powder reported in the literature [22]. This result indicates that the effective decarbonation treatment for carbonate type LDH powder is also effective for the present LDH solid film. Figure 5(c) shows the XRD pattern of the LDH solid film obtained after immersing the AcO⁻ type LDH solid film into Pyr⁻ ethanol solution. In this XRD pattern, the new diffraction peak could

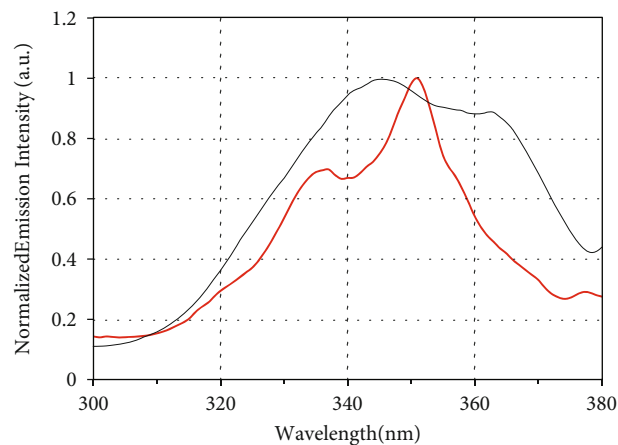


FIGURE 8: Normalized excitation spectra of the Pyr⁻/LDH hybrid film monitored at 400 nm (red line) and 460 nm (black line).

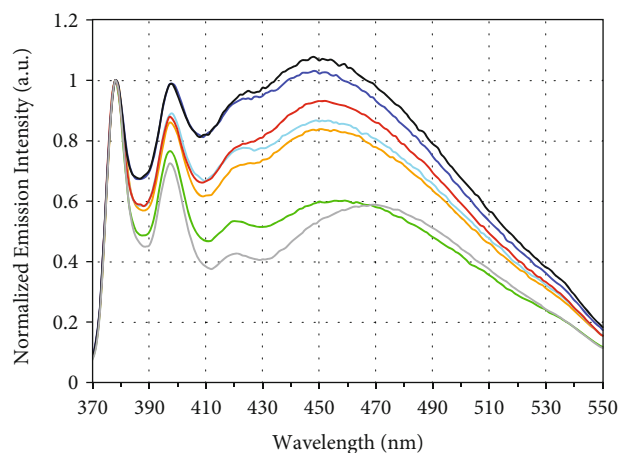


FIGURE 9: Emission spectra of the Pyr⁻/LDH film immersed in toluene-ethanol solution (concentration of toluene (v/v) are 0%: black line, 10%: blue line, 30%: red line, 50%: sky-blue line, 70%: orange line, 90%: green line, and 100%: gray line).

be observed without that from carbonate type and/or AcO⁻ type LDHs. This result indicates that the Pyr⁻ anions can be incorporated in the LDH solid film via anion-exchange reaction. However, the interlayer space (0.34 nm) calculated from this peak was larger than the interlayer space (0.31 nm) of carbonate type LDH film and smaller than the thickness of Pyr⁻ considering the diameter of sulfonate and thickness of aromatic ring (ca. 0.5 nm) [27, 28]. Thus, there are both Pyr⁻ and carbonate anions in the present Pyr⁻/LDH solid film. This can be supported by small amount of incorporated Pyr⁻ anions in the Pyr⁻/LDH solid film (0.14%vsAEC), which was calculated from absorbance of residual Pyr⁻ anion in filtrate obtained after the immersing process.

In Figure 6, photographs of Pyr⁻/LDH solid films under (a) room light, (b) UV irradiation (365 nm), and (c) absorption spectra of Pyr⁻ aqueous solution and Pyr⁻/LDH film are shown.

As see in Figure 6(a), the transparency of the Pyr⁻/LDH solid film was kept after both decarbonation and

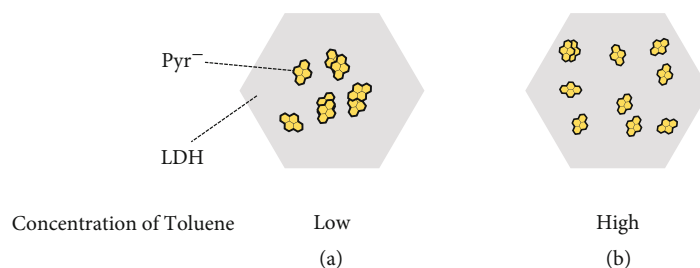


FIGURE 10: Schematic view of Pyr^- in the interlayer of LDH (a) in air and (b) in the ethanol-toluene mixed solvent.

hybridization of Pyr^- anions, and then strong sky-blue color emission, which is known as typical excimer emission of pyrene derivatives, could be observed by UV irradiation (365 nm) as shown in Figure 6(b). This result also indicates that Pyr^- anions were incorporated in the LDH solid film. In Figure 6(c), the new absorption band appeared around 350–390 nm in the Pyr^-/LDH film. Similar spectral change was observed in the diffuse reflectance spectra of LDH powder incorporating anionic pyrene and heptanesulfonate [7]. This result indicates the incorporation of Pyr^- in LDH although absorption spectra of the hybrid film were different from that of Pyr^- aqueous solution. As discussed later, this spectral change suggests that Pyr^- formed the aggregate in the interlayer space of LDH. The emission spectra of the Pyr^-/LDH film in air and Pyr^- aqueous solution were shown in Figure 7.

Two sharpen peaks (at 378 and 399 nm) and broaden peak (around 465 nm) were observed in emission spectra of the Pyr^-/LDH hybrid film. The maximum emission wavelength of sharpen peaks is almost the same as the emission maximum wavelength of Pyr^- in aqueous medium (377 and 396 nm), indicating that these sharpen peaks at 378 and 399 nm were emission from excited Pyr^- monomer in LDH. Emission band around 465 nm will be emission from excimer of Pyr^- judging from large red shift and peak broadening. This result indicated that emission from excimer and monomer can be observed in this system. Excitation spectra of the hybrid film monitored at 400 and 460 nm were shown in Figure 8.

Excitation spectrum observed from emission at 400 nm was almost the same as absorption spectrum of Pyr^- monomer in aqueous medium. This result indicates that the emission at 400 nm originates from the monomeric state of Pyr^- anions in the LDH solid film. On the other hand, excitation spectra observed from emission at 460 nm did not correspond to the excitation spectra observed at 400 nm, although excitation spectra of typical excimer, which is a dimer associated in an excited state, correspond to the excitation spectra monitored at monomer emission. This result indicates that the Pyr^- species with 460 nm emission have a different grand state from the monomeric Pyr^- species with 400 nm emission. This fact indicates that there will be intermolecular interaction among Pyr^- species in the grand state; that is, Pyr^- dimer will be associated in the LDH solid film. Thus, the strong excimer-like emission at around 460 nm can be explained as emission from Pyr^- dimer associated in the grand state under UV irradiation, so-called as “static

excimer” [29–32]. Additionally, peaks originated from monomeric Pyr^- was not observed in excitation spectra monitored at 460 nm, indicating the absence of typical excimer, which was called as “dynamic excimer” and which is formed by the encounter between excited pyrene and second pyrene in the grand state.

In Figure 9, the emission spectra of the Pyr^-/LDH solid film normalized by emission intensity at 400 nm after immersed in the ethanol-toluene mixed solution with various toluene content (v/v%) are shown.

The normalized intensity of emission from excimer (460 nm) decreased with an increase in the toluene content, but the peak wavelength of excimer emission did not change, even when the toluene content was varied. These results indicate that the decrease of the normalized emission intensity from excimer is caused by the decrease of abundance amount of “static excimer,” but not the change of the chemical state of incorporated Pyr^- anions.

It is known that aggregates and emission behavior of pyrene derivatives depend on their medium [33, 34]. Judging from the observed emission spectral change and this dependency, the mechanism of the decrease of emission originated from static excimer will be ascribed to the dissociation of Pyr^- aggregate by adsorption of toluene in the interlayer spaces as follows. Pyr^- associated the aggregates in ethanol or the mixed solution containing small amount of toluene because of strong hydrophobic interaction, thus static excimer can be observed (Figure 10(a)). On the other hand, when concentration of toluene was increased, toluene will be adsorbed in the interlayer space of LDH, and Pyr^- aggregates were dissociated because hydrophobic interaction is weakened by toluene adsorption (Figure 10(b)).

4. Conclusions

The LDH thin film was prepared by the FFT method, and transparency of the obtained film was enough to measure transmission spectra. It was succeeded to prepare the transparent Pyr^-/LDH hybrid film via decarbonation and anion-exchange processes, and it was revealed that intercalated Pyr^- formed emissive aggregate, which is called as static excimer. The luminous response of the transparent Pyr^-/LDH solid film was investigated in ethanol-toluene mixed solution with various toluene contents. The ratio of luminescence intensities from static excimer of incorporated Pyr^- molecules depended on the toluene content and decreased with an increase of the toluene content because of the dissociation

of Pyr⁻ aggregate by adsorption of toluene. Obtained results suggested that the present transparent hybrid film may be useful as a detectable material of toluene in solvent by luminous change.

Data Availability

The data used to support the findings of this study are available from the corresponding author upon request.

Conflicts of Interest

The authors declare that they have no conflicts of interest.

Acknowledgments

The authors are grateful to the Kyowa chemical Industry, Co., Ltd. for providing LDH. This work has been supported by Grant-in-Aid for Scientific Research (KAKENHI, No. 19K15522).

References

- [1] Q. Wang and D. O'Hare, "Recent advances in the synthesis and application of layered double hydroxide (LDH) nanosheets," *Chemical Reviews*, vol. 112, no. 7, pp. 4124–4155, 2012.
- [2] F. L. Theiss, S. J. Couperthwaite, G. A. Ayoko, and R. L. Frost, "A review of the removal of anions and oxyanions of the halogen elements from aqueous solution by layered double hydroxides," *Journal of Colloid and Interface Science*, vol. 417, pp. 356–368, 2014.
- [3] S. Miyata, "Anion-exchange properties of hydrotalcite-like compounds," *Clays and Clay Minerals*, vol. 31, no. 4, pp. 305–311, 1983.
- [4] T. Shichi and K. Takagi, "Clay minerals as photochemical reaction fields," *Journal of Photochemistry and Photobiology C: Photochemistry Reviews*, vol. 1, no. 2, pp. 113–130, 2000.
- [5] P. K. Dutta and D. S. Robins, "Pyrene sorption in organic-layered double-metal hydroxides," *Langmuir*, vol. 10, no. 6, pp. 1851–1856, 1994.
- [6] L. Mohanambe and S. Vasudevan, "Aromatic molecules in restricted geometries: pyrene excimer formation in an anchored bilayer," *The Journal of Physical Chemistry B*, vol. 110, no. 29, pp. 14345–14354, 2006.
- [7] A. L. Costa, A. C. Gomes, M. Pillinger, I. S. Gonçalves, and J. S. Seixas de Melo, "Controlling the fluorescence behavior of 1-pyrenesulfonate by cointercalation with a surfactant in a layered double hydroxide," *Langmuir*, vol. 31, no. 16, pp. 4769–4778, 2015.
- [8] F. Wypych, G. A. Bubniak, M. Halma, and S. Nakagaki, "Exfoliation and immobilization of anionic iron porphyrin in layered double hydroxides," *Journal of Colloid and Interface Science*, vol. 264, no. 1, pp. 203–207, 2003.
- [9] R. Sasai and M. Morita, "Luminous relative humidity sensing by anionic fluorescein dyes incorporated into layered double hydroxide/1-butanedisulfonate hybrid materials," *Sensors and Actuators B: Chemical*, vol. 238, pp. 702–705, 2017.
- [10] T. Fujimura, T. Shimada, R. Sasai, and S. Takagi, "Optical humidity sensing using transparent hybrid film composed of cationic magnesium porphyrin and clay mineral," *Langmuir*, vol. 34, no. 12, pp. 3572–3577, 2018.
- [11] D. Yan, J. Lu, M. Wei, D. G. Evans, and X. Duan, "Recent advances in photofunctional guest/layered double hydroxide host composite systems and their applications: experimental and theoretical perspectives," *Journal of Materials Chemistry*, vol. 21, no. 35, article 13128, 2011.
- [12] D. Yan, J. Lu, J. Ma et al., "Near-infrared absorption and polarized luminescent ultrathin films based on sulfonated cyanines and layered double hydroxide," *The Journal of Physical Chemistry C*, vol. 115, no. 16, pp. 7939–7946, 2011.
- [13] Y. He, R. Wang, T. Jiao et al., "Facile preparation of self-assembled layered double hydroxide-based composite dye films as new chemical gas sensors," *ACS Sustainable Chemistry & Engineering*, vol. 7, no. 12, pp. 10888–10899, 2019.
- [14] M. Ogawa and K. Kuroda, "Photofunctions of intercalation compounds," *Chemical Reviews*, vol. 95, no. 2, pp. 399–438, 1995.
- [15] D. M. Kaschak, J. T. Lean, C. C. Waraksa, G. B. Saupe, H. Usami, and T. E. Mallouk, "Photoinduced energy and electron transfer reactions in lamellar polyanion/polycation thin films: toward an inorganic "leaf"," *Journal of the American Chemical Society*, vol. 121, no. 14, pp. 3435–3445, 1999.
- [16] R. Sasai, Y. Kato, W. Soontornchaiyakul et al., "Photoinduced electron transfer in layer-by-layer thin solid films containing cobalt oxide nanosheets, porphyrin, and methyl viologen," *Physical Chemistry Chemical Physics*, vol. 19, no. 7, pp. 5611–5616, 2017.
- [17] Y. Nabetani, H. Takamura, Y. Hayasaka et al., "An artificial muscle model unit based on inorganic nanosheet sliding by photochemical reaction," *Nanoscale*, vol. 5, no. 8, pp. 3182–3193, 2013.
- [18] R. Liang, S. Xu, D. Yan et al., "CdTe quantum dots/layered double hydroxide ultrathin films with multicolor light emission via layer-by-layer assembly," *Advanced Functional Materials*, vol. 22, no. 23, pp. 4940–4948, 2012.
- [19] J. Kawamata, Y. Suzuki, and Y. Tenma, "Fabrication of clay mineral-dye composites as nonlinear optical materials," *Philosophical Magazine*, vol. 90, no. 17-18, pp. 2519–2527, 2010.
- [20] Y. Suzuki, Y. Tenma, Y. Nishioka, K. Kamada, K. Ohta, and J. Kawamata, "Efficient two-photon absorption materials consisting of cationic dyes and clay minerals," *The Journal of Physical Chemistry C*, vol. 115, no. 42, pp. 20653–20661, 2011.
- [21] Y.-h. Aoyama, T. Fujimura, and R. Sasai, "Preparation of α -zirconium phosphate nanosheet stacked solid films with high transparency and intercalating with cationic free-base porphyrins," *Chemistry Letters*, vol. 48, no. 1, pp. 40–42, 2019.
- [22] N. Iyi, Y. Ebina, and T. Sasaki, "Water-swallowable MgAl-LDH (layered double hydroxide) hybrids: synthesis, characterization, and film preparation," *Langmuir*, vol. 24, no. 10, pp. 5591–5598, 2008.
- [23] A. Mohr, P. Talbiersky, H. G. Korth et al., "A new pyrene-based fluorescent probe for the determination of critical micelle concentrations," *The Journal of Physical Chemistry B*, vol. 111, no. 45, pp. 12985–12992, 2007.
- [24] Y. Niko, S. Kawauchi, and G. Konishi, "Solvatochromic pyrene analogues of prodan exhibiting extremely high fluorescence quantum yields in apolar and polar solvents," *Chemistry A European Journal*, vol. 19, no. 30, pp. 9760–9765, 2013.

- [25] D. Kim, R. Amos, M. Gauthier, and J. Duhamel, "Applications of pyrene fluorescence to the characterization of hydrophobically modified starch nanoparticles," *Langmuir*, vol. 34, no. 29, pp. 8611–8621, 2018.
- [26] R. Sasai, H. Sato, M. Sugata et al., "Why do carbonate anions have extremely high stability in the interlayer space of layered double hydroxides? Case study of layered double hydroxide consisting of mg and Al (mg/Al = 2)," *Inorganic Chemistry*, vol. 58, no. 16, pp. 10928–10935, 2019.
- [27] H. Jiang, J. M. Leger, and I. Huc, "Aromatic δ -peptides," *Journal of the American Chemical Society*, vol. 125, no. 12, pp. 3448–3449, 2003.
- [28] Y. Marcus, "Ionic radii in aqueous solutions," *Chemical Reviews*, vol. 88, no. 8, pp. 1475–1498, 1988.
- [29] F. M. Winnik, "Photophysics of preassociated pyrenes in aqueous polymer solutions and in other organized media," *Chemical Reviews*, vol. 93, no. 2, pp. 587–614, 1993.
- [30] P. K. Lekha and E. Prasad, "Tunable emission of static excimer in a pyrene-modified polyamidoamine dendrimer aggregate through positive solvatochromism," *Chemistry A European Journal*, vol. 17, no. 31, pp. 8609–8617, 2011.
- [31] Y. Ohishi and M. Inouye, "Circularly polarized luminescence from pyrene excimers," *Tetrahedron Letters*, vol. 60, no. 46, article 151232, 2019.
- [32] C. V. Kumar, E. H. Asuncion, and G. Rosenthal, "Static pyrene excimer formation at hydrophobic zirconium phosphate surfaces: the salt effect," *Microporous Materials*, vol. 1, no. 5, pp. 299–308, 1993.
- [33] S. C. Deshmukh, S. Rana, S. V. Shinde, B. Dhara, N. Ballav, and P. Talukdar, "Selective sensing of metal ions and nitro explosives by efficient switching of excimer-to-monomer emission of an amphiphilic pyrene derivative," *ACS Omega*, vol. 1, no. 3, pp. 371–377, 2016.
- [34] T. A. Sherstneva, K. P. Birin, and V. V. Arslanov, "The aggregation behavior of amphiphilic pyrene chromophore in solutions and Langmuir monolayers," *Protection of Metals and Physical Chemistry of Surfaces*, vol. 49, no. 1, pp. 66–79, 2013.